

**NUCLEAR DATA AND MEASUREMENTS SERIES**

**ANL/NDM-136**

**Neutron Scattering and Models: Iron**

by

A.B. Smith

August 1995

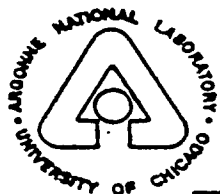
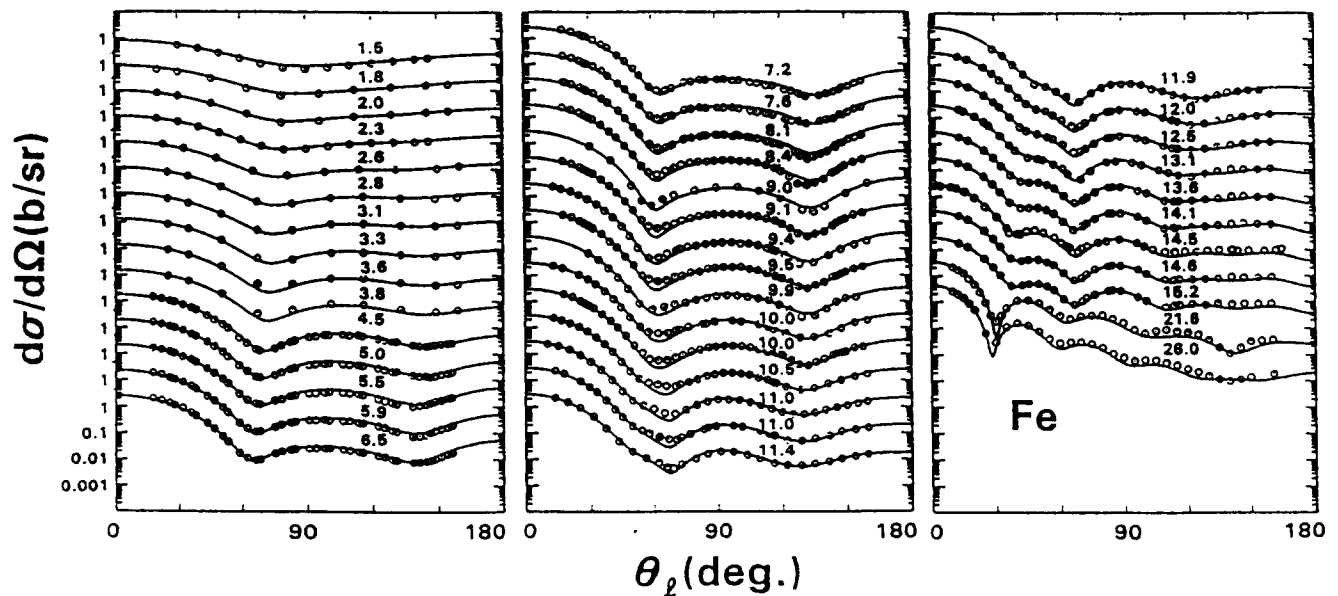
**ARGONNE NATIONAL LABORATORY,  
ARGONNE, ILLINOIS 60439, U.S.A.**

# NUCLEAR DATA AND MEASUREMENTS SERIES

ANL/NDM - 136

NEUTRON SCATTERING AND MODELS:- IRON

A. B. Smith  
August, 1995



ARGONNE NATIONAL LABORATORY, ARGONNE, ILLINOIS

Operated by THE UNIVERSITY OF CHICAGO

for the U. S. DEPARTMENT OF ENERGY

under Contract W-31-109-Eng-38

Argonne National Laboratory, with facilities in the states of Illinois and Idaho, is owned by the United States government, and operated by The University of Chicago under the provisions of a contract with the Department of Energy.

#### **DISCLAIMER**

This report was prepared as an account of work sponsored by an agency of the United States Government. Neither the United States Government nor any agency thereof, nor any of their employees, makes any warranty, express or implied, or assumes any legal liability or responsibility for the accuracy, completeness, or usefulness of any information, apparatus, product, or process disclosed, or represents that its use would not infringe privately owned rights. Reference herein to any specific commercial product, process, or service by trade name, trademark, manufacturer, or otherwise, does not necessarily constitute or imply its endorsement, recommendation, or favoring by the United States Government or any agency thereof. The views and opinions of authors expressed herein do not necessarily state or reflect those of the United States Government or any agency thereof.

Reproduced from the best available copy.

Available to DOE and DOE contractors from the  
Office of Scientific and Technical Information  
P.O. Box 62  
Oak Ridge, TN 37831  
Prices available from (615) 576-8401

Available to the public from the  
National Technical Information Service  
U.S. Department of Commerce  
5285 Port Royal Road  
Springfield, VA 22161

ANL/NDM-136

NEUTRON SCATTERING AND MODELS:- IRON<sup>\*</sup>

by

A. B. Smith

Argonne National Laboratory  
Argonne, Illinois

and

The University of Arizona  
Tucson, Arizona

August, 1995

---

Keywords:

Measured  $d\sigma/d\Omega_{el}$  and  $d\sigma/d\Omega_{inel}$  (4.5-10 MeV) for neutrons incident on elemental iron. Comprehensive optical and coupled-channels model interpretations.

---

-----  
<sup>\*</sup> This work supported by the United States Department of Energy under contract W-31-109-Eng-38, and by the Department of Nuclear and Energy Engineering, College of Engineering and Mines, University of Arizona.

## PUBLICATIONS IN THE ANL/NDM SERIES

A listing of recent issues in this series is given below. Issues and/or titles prior to ANL/NDM-120 can be obtained from the National Technical Information Service, U. S. Department of Commerce, 5285 Port Royal Road, Springfield, VA 22161, or by contacting the author of this report at the following address:-

Technology Development Division  
Argonne National Laboratory  
9700 South Cass Avenue  
Argonne, IL 60439  
USA

- A. B. SMITH, P. T. GUENTHER, J. F. WHALEN, AND S. CHIBA  
*Fast-neutron Total and Scattering Cross Sections of  $^{58}\text{Ni}$  and Nuclear Models*  
ANL/NDM-120, July 1991
- S. CHIBA AND D. L. SMITH  
*A Suggested Procedure for Resolving an Anomaly in Least-squares Data Analysis Known as "Peelle's Pertinent Puzzle" and the General Implications for Nuclear Data Evaluation*  
ANL/NDM-121, September 1991
- D. L. SMITH AND DOMINIQUE FEAUTRIER  
*Development and Testing of a Deuterium Gas Target Assembly for Neutron Production Via the  $\text{H-2}(D,N)\text{He-3}$  Reaction at a Low-energy Accelerator Facility*  
ANL/NDM-122, March 1992
- D. L. SMITH AND E. T. CHENG  
*A Review of Nuclear Data Needs and Their Status for Fusion Reactor Technology with some Suggestions on a Strategy to Satisfy the Requirements*  
ANL/NDM-123, September 1991
- J. W. MEADOWS  
*The Thick-Target  $^9\text{Be}(d,n)$  Neutron Spectra for Deuteron Energies Between 2.6 and 7.0-MeV*  
ANL/NDM-124, November 1991
- A. B. SMITH AND P. T. GUENTHER  
*Fast-Neutron Scattering Near Shell Closures:- Scandium*  
ANL/NDM-125, August 1992
- A. B. SMITH, J. W. MEADOWS AND R. J. HOWERTON  
*A Basic Evaluated Neutronic Data File for Elemental Scandium*  
ANL/NDM-126, November 1992

- A. B. SMITH AND P. T. GUENTHER  
*Fast-Neutron Interaction With Vibrational Cadmium Nuclei*  
 ANL/NDM-127, November 1992
- D. L. SMITH  
*A Least-Squares Computational "Tool Kit"*  
 ANL/NDM-128, April 1993
- JOSEPH McCABE, A. B. SMITH AND J. W. MEADOWS  
*Evaluated Nuclear Data Files for the Naturally-Occurring Isotopes of Cadmium*  
 ANL/NDM-129, June 1993
- A. B. SMITH AND P. T. GUENTHER  
*Fast-Neutron Interaction with the Fission Product  $^{109}\text{Rh}$*   
 ANL/NDM-130, September 1993
- A. B. SMITH AND P. T. GUENTHER  
*Fast-Neutron Scattering from Vibrational Palladium Nuclei*  
 ANL/NDM-131, October 1993
- A. B. SMITH  
*Neutron Interaction with Doubly-Magic  $^{40}\text{Ca}$*   
 ANL/NDM-132, December 1993
- A. B. SMITH  
*Neutron Scattering at  $Z = 50$ :- Tin*  
 ANL/NDM-133, September 1994
- A. B. SMITH, S. CHIBA AND J. W. MEADOWS  
*An Evaluated Neutronic File for Elemental Zirconium*  
 ANL/NDM-134, September 1994
- A. B. SMITH  
*Neutron Scattering from Elemental Uranium and Thorium*  
 ANL/NDM-135, February 1995

## TABLE OF CONTENTS

Abstract .....	1
1. Introduction .....	2
2. Measurement Methods .....	3
3. Experimental Results	
3.1. Elastic Neutron Scattering .....	4
3.2. Inelastic Neutron Scattering .....	7
4. Physical Models	
4.1. Data Base .....	8
4.2. Potential Forms .....	12
4.3. The Spherical Optical Model .....	12
4.4. The Coupled-Channels Model .....	16
5. Discussion and Summary	
5.1. Comparison of ISOM, ESOM, CCVIB and CCROT Potentials .....	31
5.2. Comparison of Phenomenological Potentials .....	33
5.3. Equation of State .....	34
5.4. Total Cross Sections .....	34
5.5. Differential Elastic Scattering .....	35
5.6. Differential Inelastic Scattering .....	36
5.7. Strength Functions .....	36
5.8. Scattered-neutron Polarization .....	37
5.9. Deformation and Coupling .....	40
5.10. Asymmetry .....	41
5.11. Microscopic Models .....	42
5.12. Dispersion Effects .....	44
5.13. Summary Comments .....	47
Acknowledgements .....	48
Appendix A. PTB Data Interpretations .....	48
Appendix B. Pseudo-data Fitting .....	55
References .....	60

NEUTRON SCATTERING AND MODELS:- IRON

by

A. B. Smith

Argonne National Laboratory  
Argonne, Illinois  
and  
The University of Arizona  
Tucson, Arizona

ABSTRACT

Differential elastic and inelastic neutron-scattering cross sections of elemental iron are measured from 4.5 to 10 MeV in increments of  $\approx 0.5$  MeV. At each incident energy the measurements are made at forty or more scattering angles distributed between  $\approx 17^\circ$  and  $160^\circ$ , with emphasis on elastic scattering and inelastic scattering due to the excitation of the yrast  $2^+$  state. The measured data is combined with earlier lower-energy results from this laboratory, with recent high-precision  $\approx 9.5 \rightarrow 15$  MeV results from the Physikalisch-Technische Bundesanstalt and with selected values from the literature to provide a detailed neutron-scattering data base extending from  $\approx 1.5$  to 26 MeV. This data is interpreted in the context of phenomenological spherical-optical and coupled-channels (vibrational and rotational) models, and physical implications discussed. Deformation, coupling, asymmetry and dispersive effects are explored. It is shown that, particularly in the collective-rotational context, a good description of the interaction of neutrons with  $^{56}\text{Fe}$  is achieved over the energy range  $\approx 0 \rightarrow 30$  MeV, avoiding the dichotomies between high and low-energy interpretations found in previous work.



## 1. INTRODUCTION

Iron, in the form of a variety of alloys, is the major structural material for the large majority of fission and fusion nuclear-energy systems. Thus, for more than half a century neutron scattering from elemental iron has been studied. At lower and resonance energies, neutron scattering provides a signature of resonance spins and parities (e.g., ref. [Per+77]). At somewhat higher energies it is no longer technologically possible to resolve scattering from individual resonances, and what is observed is a fluctuating cross section, with a periodicity and width of the order of 100 keV. Measurements in this fluctuating region must be made in great detail if the energy-average behavior is to be determined. At still higher energies the resonances broaden and strongly overlap, and the cross sections smooth to energy-dependent trends consistent with the concept of an optical or a coupled-channels model. Cross sections have been determined in the fluctuating region with sufficient detail to permit the derivation of energy-averaged behavior (e.g., refs. [SG80] and [Bar+68]). There have been a number of measurements reported in the higher-energy and non-fluctuating region (e.g., refs. [AHW66], [BLS71], [Coo+58], [ElK+82], [Fer+77], [GT65], [Han+84], [Hol+69], [Kin68], [KP70], [Mel+83], [OTR90], [Ols+87], [Ram75], [RSL67], [Sal81] and [Vel+74]), but they have been made at isolated (or several) energies, and the results are not always consistent. Above  $\approx 15$  MeV the data becomes sparse and limited to several incident energies. Above  $\approx 26$  MeV there is essentially no experimental scattering information.

The present measurements were undertaken to improve the experimental knowledge of neutron scattering from iron in the transitional region from  $\approx 4 \rightarrow 10$  MeV. Concurrently, very precise and detailed measurements at the Physikalisch-Technische Bundesanstalt (herein referred to as "PTB") provide unique new experimental information from  $\approx 9.5$  to 15 MeV [Sch94]. With this new information it is now possible to construct a high quality neutron-scattering data base for iron from  $\approx 1.5$  to 15 MeV, extended to 26 MeV with several results reported in the literature. This new experimental scope and quality offers the potential for much improved model definition and physical understanding. The present work had those goals.

Elemental iron consists very largely of the isotopes  $^{54}\text{Fe}$  (5.9% abundant) and  $^{56}\text{Fe}$  (91.72% abundant). Both are pf-shell nuclei with the former having a closed neutron shell ( $N = 28$ ) and the latter two neutrons beyond the closed shell. Thus it is expected that the collective neutron interactions with the isotopes (vibrational or rotational) are primarily with the proton core. Both isotopes have a yrast ( $2^+$ ) level at  $\approx 1$  MeV, and coulomb-excitation studies lead to  $\beta_2$  values of  $\approx 0.24$  for the primary  $^{56}\text{Fe}$  isotope [Ram+87]. This is a relatively large value and thus one can expect significant collective direct reactions. Their implications on neutron scattering have been examined in several studies (e.g., [Del+82]), usually assuming a collective vibrational mechanism. However, shell-model studies

indicate that the low-lying structure of  $^{56}\text{Fe}$  is characteristic of a prolate rotor ([MR79], [LWS81]) but only one interpretation of neutron scattering gives consideration to this property. Both isotopes lie near the maximum of the s-wave strength function and the minimum of the p-wave strength function. The large majority of the interpretations of neutron scattering from elemental or isotopic iron is based upon data at energies of  $\approx 10$  MeV or above. The resulting reaction models do not reasonably extrapolate to the low-energy region. This dichotomy between low- and high-energy models has been long known, but unresolved as a detailed data base making the transition between the two energy regimes was not available. The problem is further complicated by fluctuating structure extending to relatively high incident energies and, possibly, by dispersive effects that have thus far received no attention despite the fact that they will be primarily felt in the lower-energy region [Sat83]. Thus, while there has been extensive study of neutron scattering from iron and its isotopes a number of outstanding physical questions persist.

This report presents new experimental results of considerable scope and addresses their physical implications in a broad context. Section 2 very briefly outlines the experimental methods. Section 3 presents the present experimental results. In Section 4 a comprehensive neutron-scattering data base is defined and discussed in the context of spherical-optical and coupled-channels models, the latter including both vibrational and rotational couplings. Finally, in Section 5 some physical implications of the measurements and their interpretations are set forth.

## 2. MEASUREMENT METHODS

The measurements were made using the fast time-of-flight technique [CL55] and the Argonne 10-angle neutron-scattering apparatus [Smi+67]. This technique and apparatus have long been used at this laboratory, and are extensively described elsewhere [Smi+92]. Therefore, only details specific to the present measurements will be given here.

All of the measurements employed a 2 cm diameter 2 cm long sample of elemental, high-purity, metallic iron. Neutrons were produced using the  $\text{D(d,n)}^3\text{H}$  reaction [Dro87] with the deuterium contained in an  $\approx 2$  cm long gas cell. The mean neutron energy was determined to  $\approx 10$  keV by magnetic analysis of the incident deuteron beam. Incident-neutron energy spreads varied from  $\approx 300$  keV at 4.5 MeV to  $\approx 100$  keV at 10 MeV. The incident deuteron beam was pulsed at a repetition rate of 2 MHz to provide neutron bursts of  $\approx 1$  nsec duration. The measurement sample was placed  $\approx 18$  cm from the neutron source at a  $0^\circ$  reaction angle and at the focus of the scattered-neutron collimator system consisting of ten scattered-neutron flight paths of  $\approx 5$  m length. In a few cases at higher energies the flight paths were extended to  $\approx 16$  m in order to improve the scattered-neutron resolution. The relative scattering

angles were optically determined to  $< 0.1^\circ$ , and the normalization of the relative angular scale determined to  $\approx 0.1^\circ$  by observing scattering both right and left of the center line. The scattered-neutron detectors were liquid scintillators whose relative energy responses were calibrated using the prompt fission-neutron spectrum of  $^{252}\text{Cf}$  [SGS77]. The effective scattered-neutron energy resolution was sufficient to resolve the elastically-scattered neutron component from inelastically-scattered contributions up to the maximum  $\approx 10$  MeV incident-neutron energy of the present experiments. All of the iron cross sections were determined relative to the well known  $\text{H}(n,n)$  scattering standard [CSL82]. The resulting cross sections were corrected for angular-resolution, beam-attenuation and multiple-event effects using Monte-Carlo calculational techniques [Smi91]. Even though the sample was small, multiple-event corrections could be large, (for example, the corrections were approximately a factor of two at the first minimum of the 10 MeV elastic-scattering distribution). Therefore, the corrections were given careful attention. It is interesting to note that the corrections used in the present work are in good agreement with those obtained at PTB using an entirely different method [Sch94].

### 3. EXPERIMENTAL RESULTS

#### 3.1. Elastic neutron scattering

The differential elastic-scattering measurements were made from 4.5 to 10 MeV in steps of  $\approx 0.5$  MeV. A minimum of forty scattering angles were used, distributed between  $\approx 17^\circ$  and  $160^\circ$ . The experimental results are summarized in Fig. 3.1.1. The uncertainties associated with these differential values ranged from  $\approx 3\%$  at forward scattering angles to larger values in the minima of the distributions. These uncertainties were inclusive of systematic normalization contributions, statistical contributions, the effects of angular uncertainties and estimated contributions due to correction procedures.

There have been a number of elemental and  $^{56}\text{Fe}$  elastic-scattering results reported in the literature that are comparable with the present results. They are of varying scope and quality. Despite some short comings, the agreement with the present results is reasonably good, as illustrated in Fig. 3.1.2. In these illustrated comparisons the differences between measured values are not large but they can have a significant impact on the subsequent model interpretations of Section 4, below.

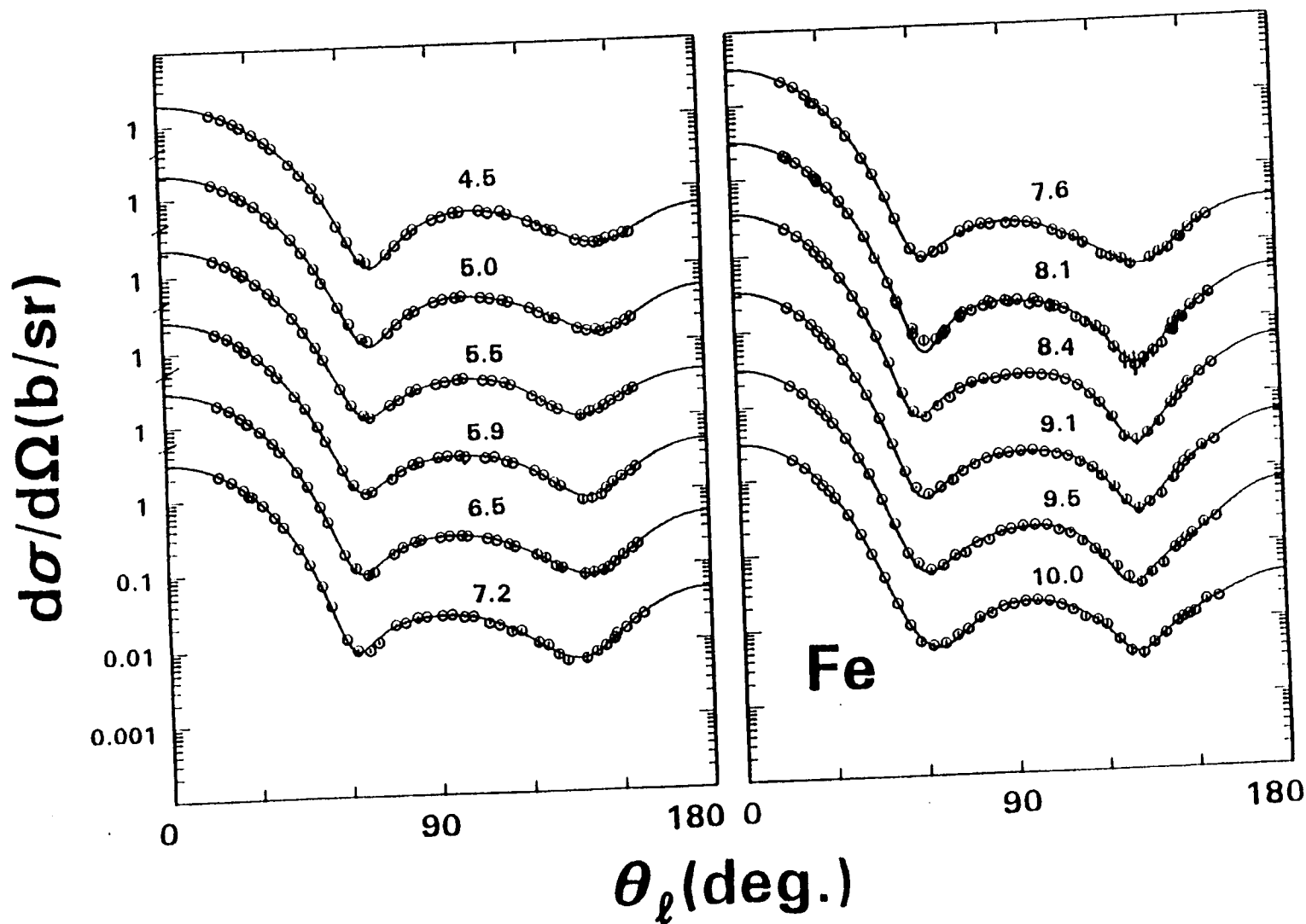


Fig. 3.1.1. Measured differential elastic-scattering cross sections of elemental iron. The present experimental results are indicated by symbols, and curves are "eye guides" obtained by fitting the distributions with Legendre-polynomial series. Approximate incident energies are numerically noted in MeV. (Throughout this paper all angular distributions are given in the laboratory coordinate system.)

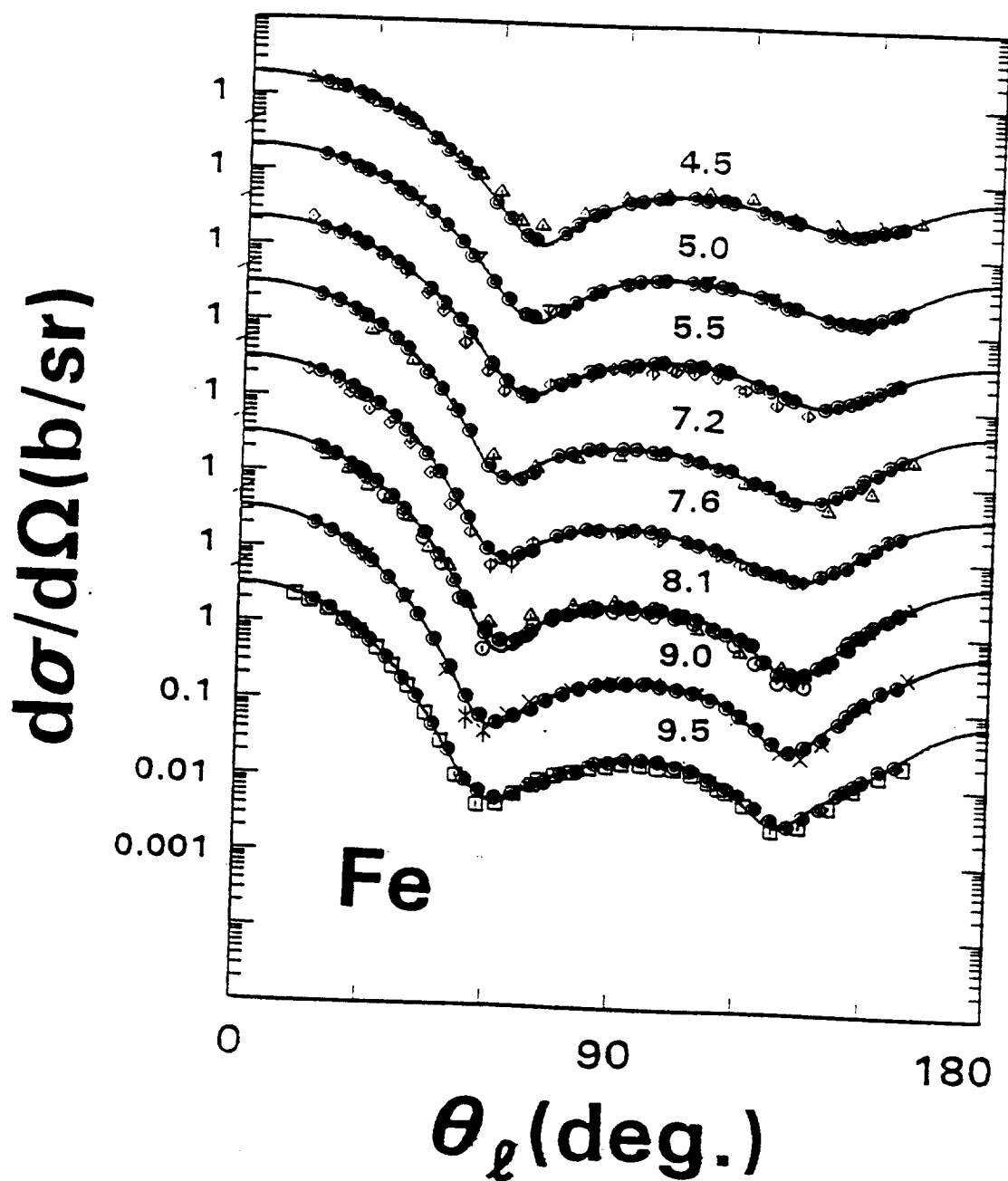


Fig. 3.1.2. Comparisons of measured iron elastic-scattering results. The present values are indicated by concentric circular data symbols. Other data symbols indicate results taken from the literature ([Sch94], [Hol+69], [BLS71], [XP70], [ELK+82], [Vel+74]). Curves are "eye-guides" constructed from the present results. Approximate incident-neutron energies are numerically noted in MeV.

### 3.2. Inelastic neutron scattering

Differential inelastic-scattering cross sections were determined concurrently with the elastic-scattering measurements, with the addition of measurements using  $\approx 16$  m flight paths to improve scattered-neutron resolutions at higher energies. Scattered neutron groups corresponding to nine excitations were observed. Only the first four of these were clearly associated with discrete excited states in iron, and the remainder consisted of contributions from several reported excited levels. Throughout this paper the excited levels of iron are assumed to be those given by the Nuclear Data Sheets ([Jun+87, Gon+87]) where the adopted values are generally taken from other reaction studies that provide better energy definition than neutron scattering. Furthermore, all the present inelastic-scattering cross sections are referenced to elemental iron, and appropriate multiplicative factors must be applied for conversion to isotopic values.

The first, and by far the more prominent, excitation was attributed to the yrast  $0.847(2^+)$  MeV level in  $^{56}\text{Fe}$ . A very weak neutron group was observed at a somewhat higher excitation energy corresponding to the  $1.408(2^+)$  MeV level in  $^{54}\text{Fe}$ . This and all other possible  $^{54}\text{Fe}$  inelastic contributions were ignored throughout this work. The next excitation corresponded to the  $2.085(4^+)$  MeV level in  $^{56}\text{Fe}$ , followed by a group attributed to the  $2.659(2^+)$  MeV level. A broad neutron group was observed corresponding to an excitation of  $\approx 3.0$  MeV. It was attributed to contributions from reported  $2.942(0^+)$ ,  $2.960(2^+)$ ,  $3.070(3^-)$ ,  $3.120(1^+)$  and  $3.123(4^+)$  MeV levels in  $^{56}\text{Fe}$  (all composite excitations may include small contributions from the minor isotopes). The next observed, and broad, scattered-neutron group corresponded to an excitation of  $\approx 3.45$  MeV and was attributed to contributions from reported  $3.370(2^+)$ ,  $3.389(6^+)$ ,  $3.445(3^+)$ ,  $3.449(1^+)$ ,  $3.599(0^+)$ ,  $3.602(2^+)$  and  $3.607(0^+)$  MeV levels in  $^{56}\text{Fe}$ . An observed neutron group corresponded to an excitation of  $\approx 3.85$  MeV, with probable contributions from levels at  $3.748(2^+)$ ,  $3.756(6^+)$ ,  $3.760(?)$ ,  $3.830(2^+)$  and  $3.856(3^+)$  MeV in  $^{56}\text{Fe}$ . Two additional broad groups of scattered neutrons were observed corresponding to excitations of  $\approx 4.4$  and  $5.0$  MeV. Both of them certainly consist of a number of contributions from levels in  $^{56}\text{Fe}$  alone. At higher excitations the observed emission spectra blended into a fluctuating continuum.

Twenty to forty differential values were measured for each of the inelastically-scattered neutron groups at every incident energy. Generally, the inelastic-neutron angular distributions were symmetric about  $90^\circ$  and approached isotropy. Exceptions were the distributions associated with the excitation of the yrast  $0.847(2^+)$  MeV level which

were peaked toward forward angles, and increasingly so with incident energy. These distributions are illustrated in Fig. 3.2.1. The angle-integrated inelastic-scattering cross sections were determined by fitting the differential distributions with Legendre-polynomial expansions. In the case of the yrast ( $2^+$ ) level the fitting procedures were augmented by inserting  $0^\circ$  and  $180^\circ$  values from the coupled-channels models of Section 4 to assure a good behavior of the fit at the angular extremes. The resulting angle-integrated inelastic-scattering cross sections are illustrated in Fig. 3.2.2. Values of the cross sections for the excitation of the 0.847 MeV level are shown in a wider energy scope in Fig. 3.2.3. The uncertainties associated with both differential and angle-integrated inelastic-scattering values are subjective estimates; including consideration of statistical, normalization and resolution effects. The present inelastic-scattering angle-integrated cross sections are reasonably consistent with a number of values reported in the literature, as shown in Fig. 3.2.2. In particular, the present results extrapolate very nicely to the lower energy values obtained at this laboratory [SG80]. There is similar very good agreement with the higher-energy results of ref. [Sch94] as illustrated in Fig. 3.2.3.

#### 4. PHYSICAL MODELS

##### 4.1. Data base

The physical models were primarily based upon elemental and isotopic differential elastic-scattering cross sections. The lower-energy limit of the elastic-scattering data base was taken to be  $\approx 1.5$  MeV. There are extensive data sets at energies of less than 1.5 MeV, obtained using white- and monoenergetic-source measurement techniques (e.g., [SLW66], [Per+77]). However, in the low-energy region the cross sections strongly fluctuate with energy, even in a broad energy average, and doorway states have been reported [EM69]. These properties are not consistent with the energy-averaged models considered here. From 1.5 to 2 MeV the elastic scattering data of Tomita et al. [Tom+70] and of Smith and Guenther [SG80] were combined in the data base. From 2 to 4 MeV the data of Smith and Guenther were used. These data sets are in energy detail and should follow the fluctuations of the cross sections within the experimental resolution employed. The data below 4 MeV was averaged over  $\approx 200$  keV energy increments in order to smooth the obvious fluctuations, and to reduce the large number of experimental distributions to manageable proportions for the extensive model calculations. Above 4 MeV the elastic-scattering data base consisted of; i) the present work (4  $\rightarrow$  10 MeV), ii) the  $\approx 9$  MeV results of Velkley et al. [Vel+74], iii) a number of differential distributions throughout the range  $\approx 9.5 \rightarrow 15$  MeV by Schmidt [Sch94], iv) the 11 MeV results of Ferrer et al. [Fer+77], v) 14.5 MeV results of Coon et al. [Coo+58], and vi) a 21.6 MeV distribution by Olsson et al. [Ols+87]. In addition,  $^{56}\text{Fe}$  isotopic elastic-scattering results were used from El-Kadi et al.

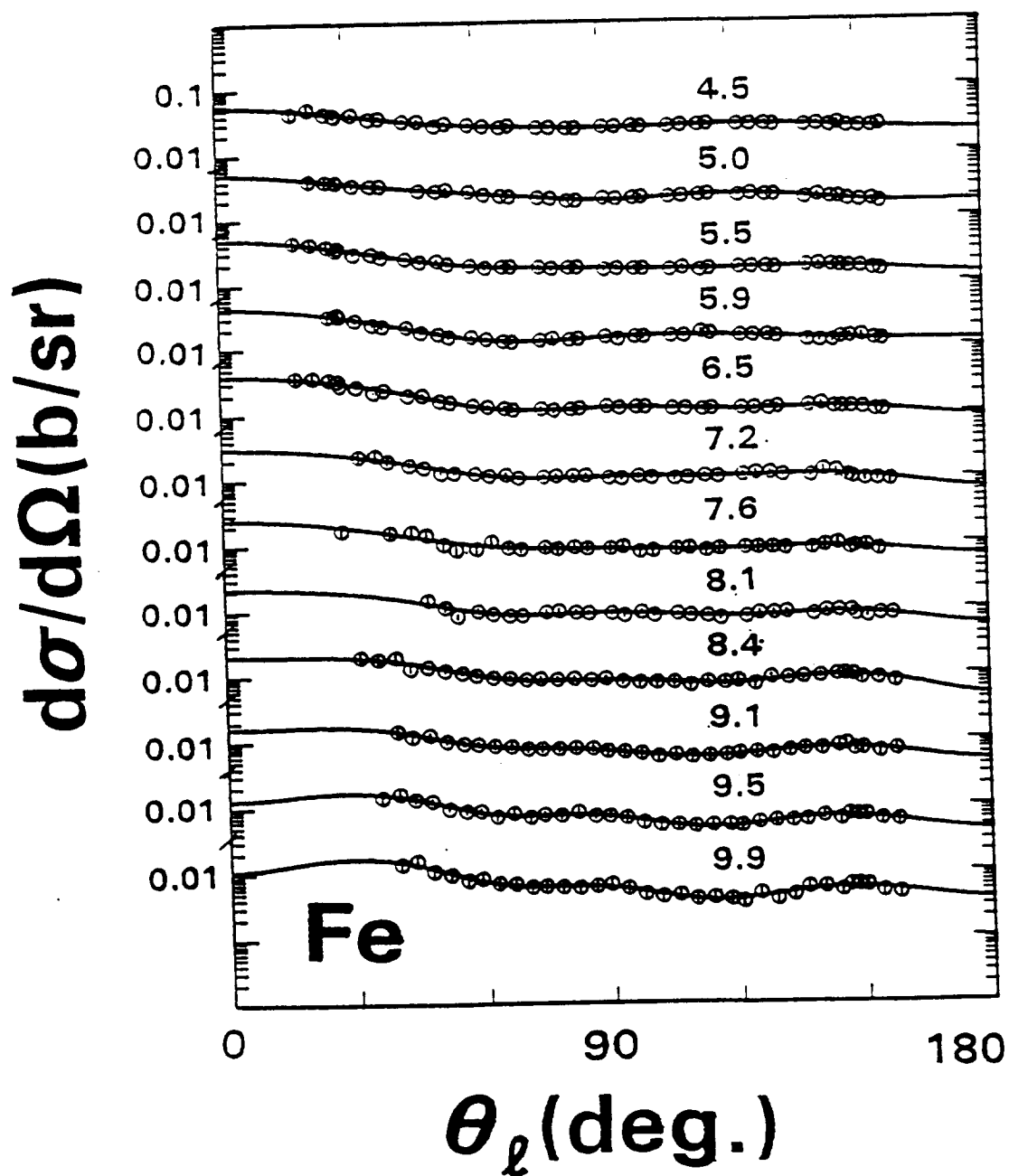


Fig. 3.2.1. The present measured (symbols) differential cross sections for the excitation of the yrast 847(2<sup>+</sup>) keV level of <sup>56</sup>Fe. Curves indicate the results of Legendre-polynomial fitting. Approximate incident energies are numerically noted in MeV.



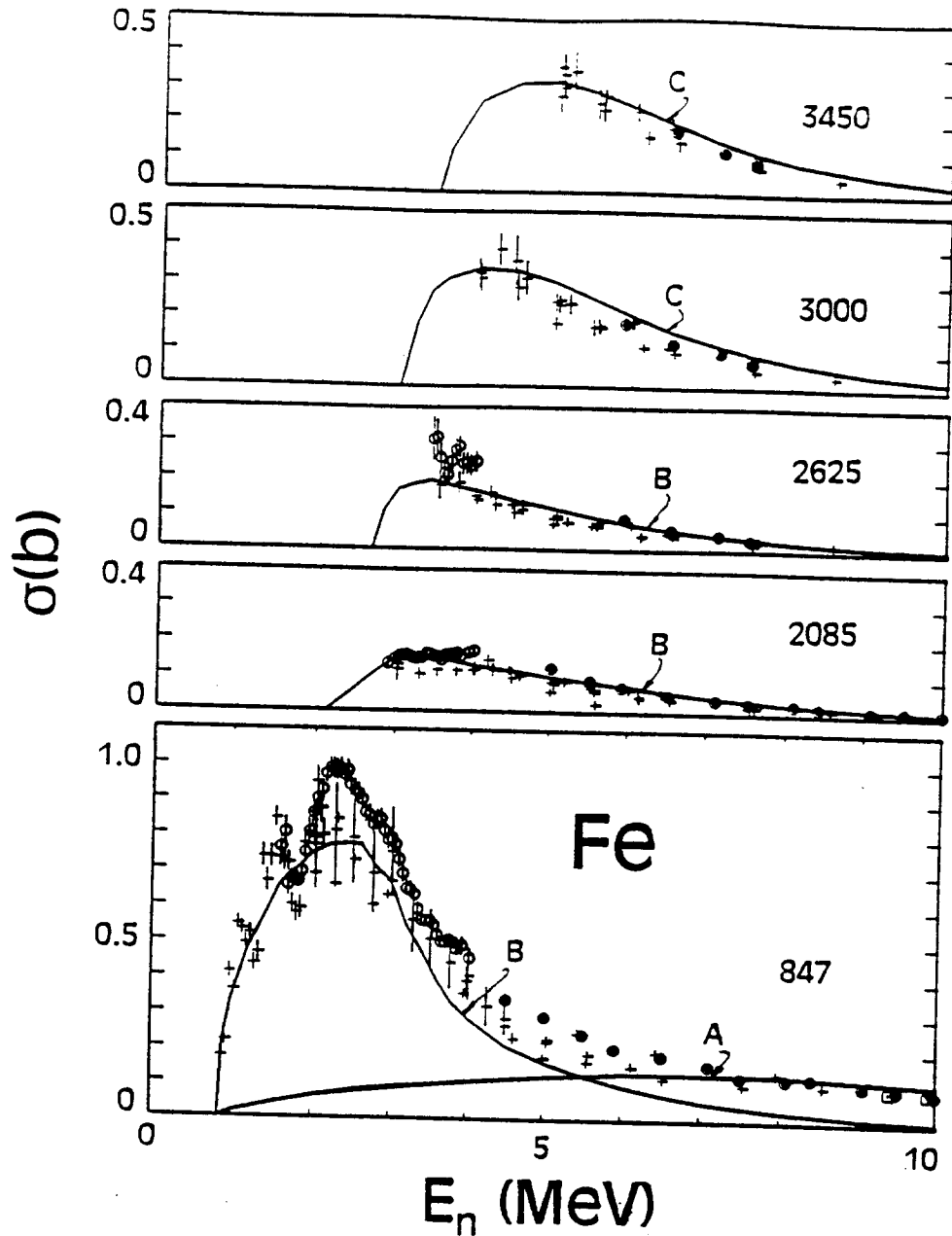


Fig. 3.2.2. Angle-integrated inelastic scattering cross sections of iron. The present results are indicated by concentric circular symbols, those from earlier work at this laboratory by circular symbols [SG80] and results from ref. [Sch94] by square symbols. Values reported elsewhere in the literature are indicated by crosses ([PKM71], [BLS71], [EIK+82], [RSL67], [AHV66], [Ram75], [GT65], [Sal81], [Kin68], [KP70]). Curves indicate model-calculated results where A denotes the direct-reaction contribution (two direct-reaction curves are shown and essentially indistinguishable, as discussed in the text), B the results of CN calculations, and C results of CN calculations for composite levels. Approximate excitation energies are numerically given in each section of the figure in keV, and all cross sections are presented on an elemental basis.

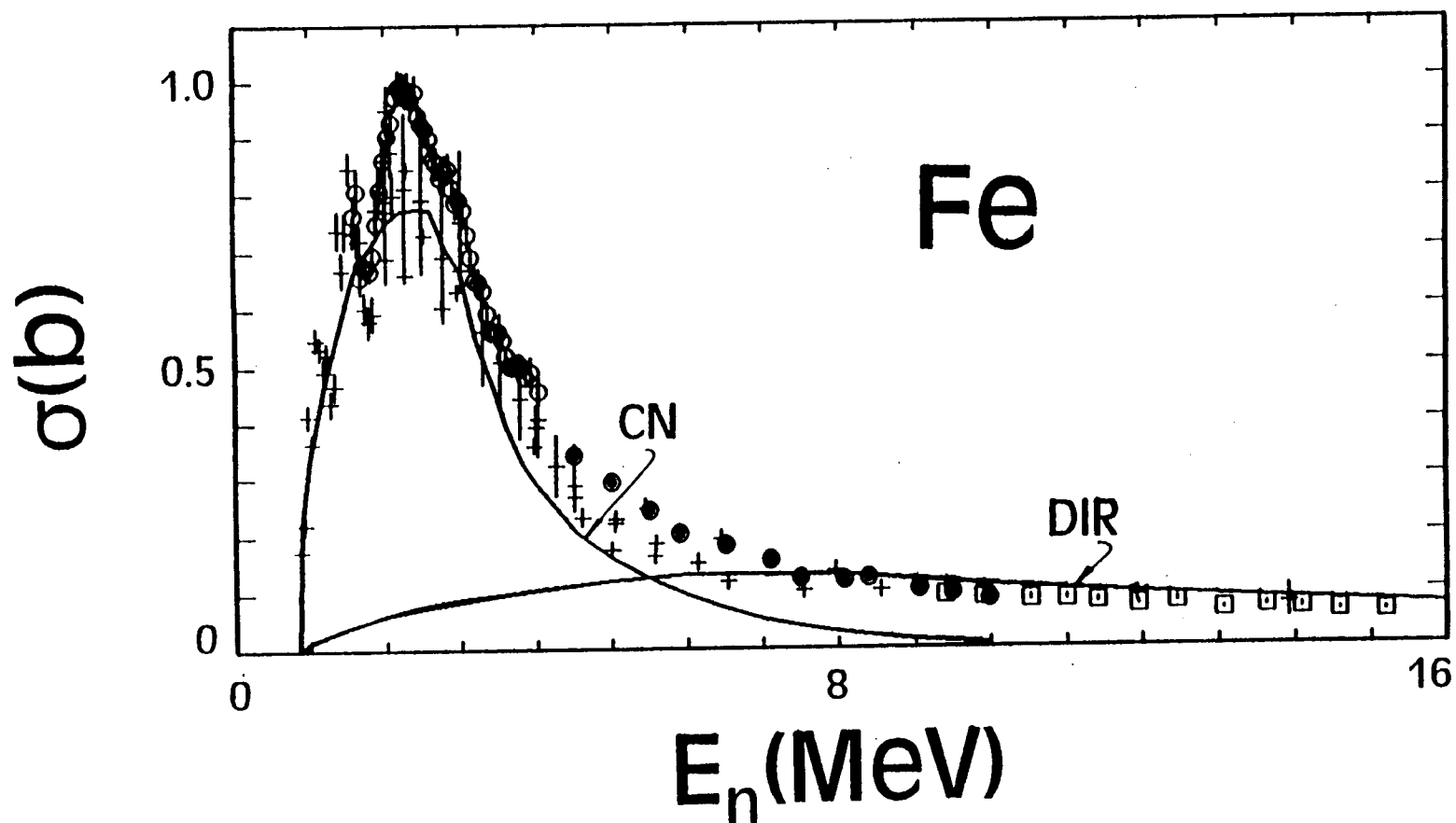


Fig. 3.2.3. Angle-integrated cross sections for the excitation of the 0.847 MeV level in  $^{56}\text{Fe}$  over an extended energy range. The notation is identical to that of Fig. 3.2.2, except that the compound-nucleus calculations are represented by the curve "CN" and those of the direct reaction by curves "DIR".

[ElK+82] at  $\approx 9, 10, 12$  and  $14$  MeV, and from Mellema et al. [Mel++83] at  $\approx 20$  and  $26$  MeV. Additional elastic-scattering data can be found in the literature, and is available from the NNDC [NNDC]. It was not used in the present physical interpretations as it was felt to be inconsistent with the body of the data base and/or was of limited angular scope or detail. The uncertainties associated with the elastic scattering were accepted as given by the various authors, although there were some systematic differences between results from various institutions beyond the stated uncertainties. The uncertainties associated with the present work are reasonably known, and those of ref. [Sch94] were given particularly careful attention. The entire elastic-scattering data base is illustrated in Fig. 4.1.1.

Consideration was also given to the neutron total cross sections, inelastic neutron scattering, strength functions and neutron elastic-scattering polarizations. The energy-averaged total cross sections were constructed from the high-resolution experimental results of Cierjacks et al. [Cie+68] and Larson [Lar80], with the results illustrated in Fig. 4.1.2. The inelastic-scattering data base was primarily taken from the present work and that of ref. [Sch94], augmented by a number of values taken from the literature ([SG80], [PK71], [BLS71], [ElK+82], [RSL67], [SLW66], [AHW66], [Ram75], [GT65], [OTR90], [Sal81]). Strength functions were taken from the compilation of ref. [MDH81]. The polarization data was limited to the work of Floyd et al. [Flo+83].

#### 4.2. Potential forms

All of the present model calculations assumed:- i) a Saxon-Woods (SW) real-potential form, ii) a SW-derivative surface-imaginary potential form and iii) a Thomas spin-orbit potential form [Hod71]. The parameters of the spin-orbit potential were taken from ref. [WG86], assuming only a real non-deformed spin-orbit strength. Where relevant, a volume-imaginary potential of the SW form with the same geometry as the real potential was used.

#### 4.3. The spherical optical model (SOM)

A simple spherical optical model is not quantitatively appropriate for a strong collective nucleus such as  $^{56}\text{Fe}$ . However, it is often a practical vehicle in both basic and applied contexts. Therefore, the SOM was initially examined in the present work. Two variants of the model were used. The simplest assumes that elemental iron consists entirely of  $^{56}\text{Fe}$ . The second approach assumes that elemental iron consists of  $^{54}\text{Fe}$  and  $^{56}\text{Fe}$ , with the relative abundances normalized to 100%. Throughout all of the interpretations the minor isotopes  $^{57}\text{Fe}$  and  $^{58}\text{Fe}$  were ignored as their total elemental abundance is  $< 2.5\%$ .

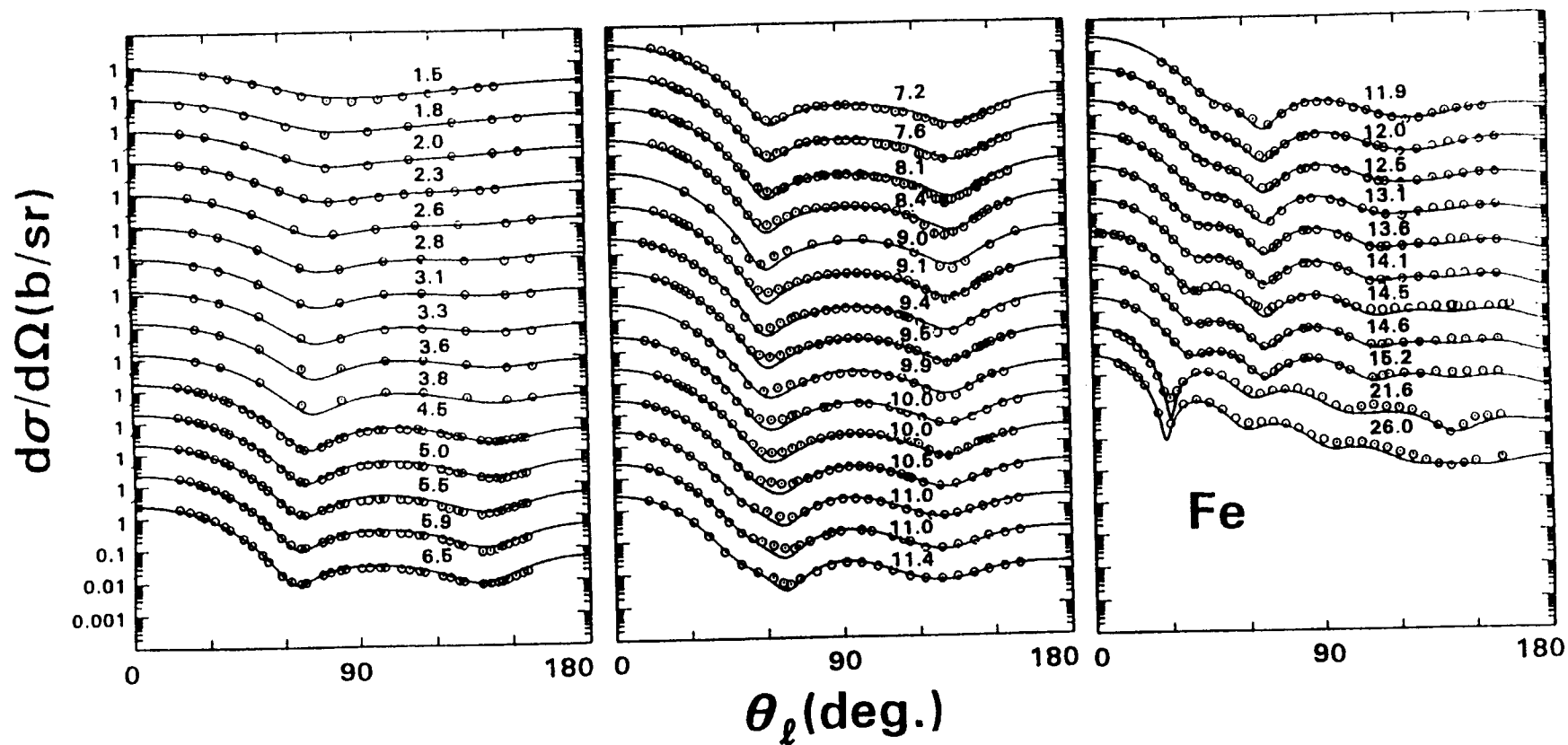


Fig. 4.1.1. The elastic-scattering data base employed in the present interpretations. Symbols indicate the experimental values, as discussed in the text, and curves the results of ISOM calculations as described in Section 4.3. Approximate energies are numerically noted in MeV.

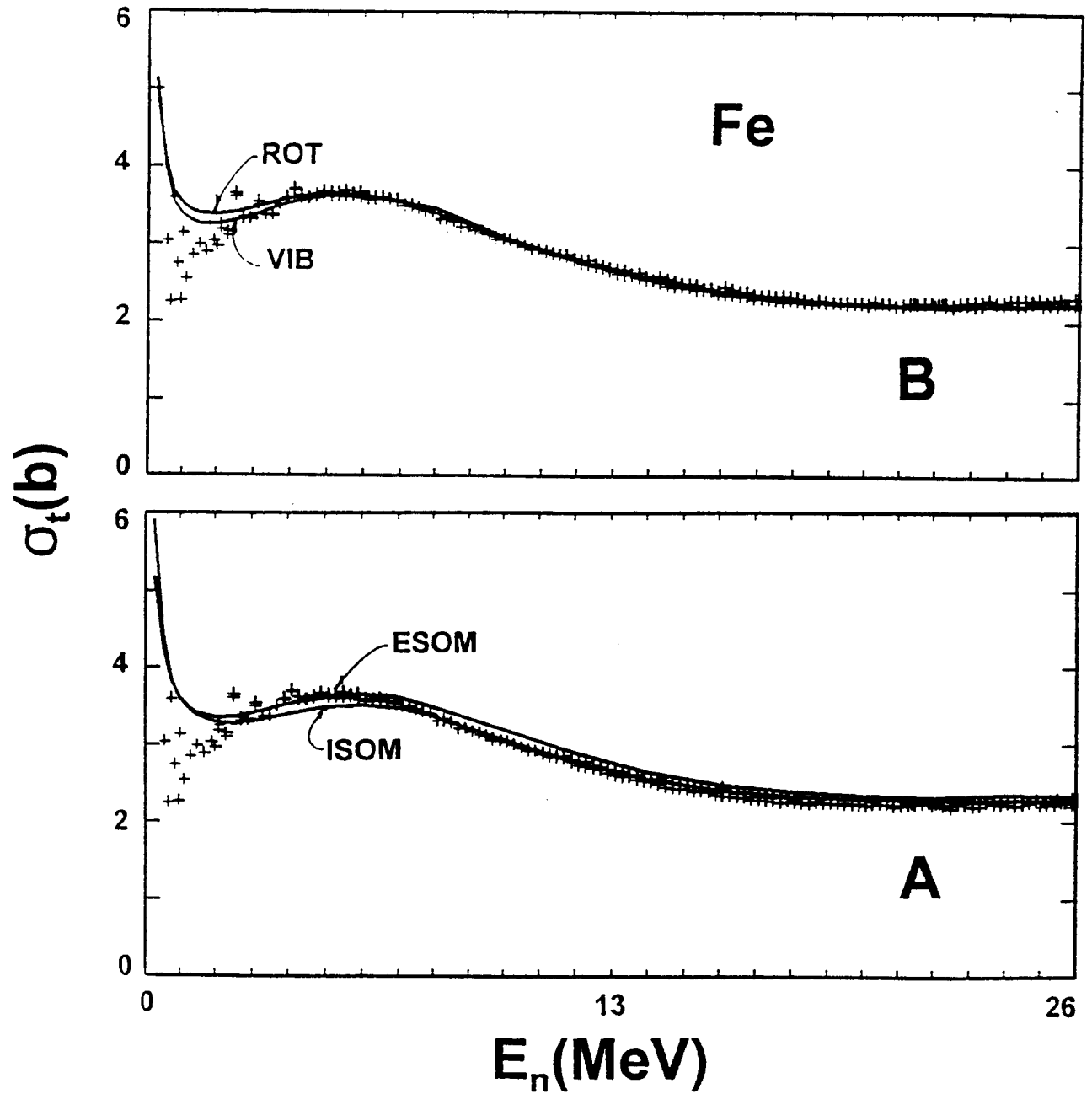


Fig. 4.1.2. Energy-averaged neutron total cross sections of elemental iron. The energy-averages of experimental values taken from refs. [Lar80] and [Cie+68] are indicated by symbols. In section "A" curves denote the results of spherical optical-model (ISOM and ESOM) calculations and in section "B" the results of coupled-channels model (VIB and ROT) calculations, as described in the text.

The parameters of all of the models were primarily determined by explicit  $\chi^2$  fitting the above elastic-scattering data base, and secondarily by subjective comparisons with broad energy averages of the measured neutron total cross sections and with s- and p-wave strength functions deduced from resonance measurements. The elastic-scattering fitting procedure followed through five steps:- i) Six parameter fitting varying real- and imaginary-potential strengths, radii, and diffusenesses. From this the real-potential diffuseness,  $a_v$ , was set at the average of the fitting results. Experience has shown  $a_v$  to be energy independent. ii) With  $a_v$  fixed, five parameter fitting was used to determine the real-potential radius,  $r_v$ . (Unless otherwise stated, throughout this report radii are presented in the reduced form,  $r_i$ , where the full radii are given by  $R_i = r_i \cdot A^{1/3}$ .) It is difficult to independently determine  $r_v$  as it is strongly correlated with the real-potential depth, however a large sample was used. iii) Four parameter fitting (with  $a_v$  and  $r_v$  fixed) was then used to determine the imaginary-potential radius,  $r_w$ . iv) Three parameter fits followed to determine the imaginary diffuseness,  $a_w$ . Again, it is difficult to independently determine  $a_w$  as it is strongly correlated with the imaginary-potential depth. v) Finally real- and imaginary-potential strengths were derived by two-parameter fitting with the geometries fixed to the values determined in the prior steps. The possible presence of volume absorption was examined at energies above 15 MeV. The assessment was made by introducing a volume-absorption potential ranging from 0  $\rightarrow$  4 MeV into the fitting procedures and searching for a minimum of  $\chi^2$ .

All of the SOM calculations were carried out using two versions of the computer code ABAREX [Mol82]. One of these simply dealt with the single isotope  $^{56}\text{Fe}$ , while the other concurrently treated the two isotopes  $^{54}\text{Fe}$  and  $^{56}\text{Fe}$  assumed to make up the elemental target. Each version explicitly treated the compound-nucleus (CN) processes using the Hauser-Feshbach formula [HF52] as modified by Moldauer for resonance width and correlation corrections [Mol80]. The necessary discrete level energies, spins and parities were taken from the Nuclear Data Sheets ([Gon+87], [Jun+87]). The statistical representation of Gilbert and Cameron [GC65] was used to represent higher-energy excitations (i.e., above excitations of  $\approx 3.8$  MeV). CN effects were explicitly treated up to incident energies of 10 MeV. At higher incident energies it was assumed that compound-elastic (CE) contributions to the elastic scattering were negligible and thus the elastic-scattering was entirely a shape-elastic (SE) process. Throughout, charged-particle reaction channels were ignored as the respective cross sections are small at energies where the CE contribution is significant.

Following the above fitting steps, and assuming that only  $^{56}\text{Fe}$  contributes to the scattering, the potential parameters of Table 4.3.1 were obtained. Herein this  $^{56}\text{Fe}$  SOM is termed the isotopic SOM or "ISOM". The description of the elastic-scattering data base obtained with the ISOM is illustrated in Fig. 4.1.1. The real-potential strength,  $J_v$ , decreases with energy in a nearly linear manner while the imaginary-potential strength falls rather sharply with energy up to  $\approx 7.5$  MeV and then is approximately constant, as illustrated in Fig. 4.3.1. Above  $\approx 12$  MeV the fitting leads to a volume absorption that increases with energy. Excepting  $a_v$ , all of the real- and imaginary-potential geometries are energy dependent.

The above ISOM ignores the 5.9% contribution from the isotope  $^{54}\text{Fe}$ . If one includes the latter isotope in the model derivation some changes can be expected, particularly at lower energies. These were examined by repeating the above fitting procedures using a special version of the code ABAREX [Mol82] that explicitly treated both the  $^{54}\text{Fe}$  and  $^{56}\text{Fe}$  isotopes. Herein the resulting potential is termed the elemental SOM, or "ESOM". The resulting potential parameters are given in Table 4.3.2. The energy dependencies of the potential strengths are shown in Fig. 4.3.2. The description of the elastic-scattering data base obtained with the ESOM is shown in Fig. 4.3.3. As one might expect, the parameters of the ESOM are similar to those of the ISOM.

#### 4.4. The coupled-channels model (CCM)

Coupled-channels model derivations using the comprehensive fitting of the ESOM, above, are prohibitively time consuming therefore some simplifying assumptions were made. First, the data base was assumed to consist only of  $^{56}\text{Fe}$ , the same assumption as for the ISOM. Compound-nucleus processes were rigorously treated up to incident energies of 4 MeV. From 4 to 10 MeV the elastic-scattering data base was corrected for compound-elastic contributions, using the above ESOM, to obtain an elastic-scattering data set that could be treated as SE scattering. The corrections were small at 4.5 MeV and decreased with increasing energy. Above 10 MeV the elastic scattering was assumed to be entirely a shape-elastic process. This adjusted elastic-scattering data base used in the CCM fitting is shown in Fig. 4.4.1.

$^{56}\text{Fe}$  is not a simple structure and clearly is of a collective nature. It is common to assume it is a simple vibrator similar to  $^{54}\text{Fe}$  [Del+82] though the quadrupole moment is far from zero. Coulomb-excitation and shell-model studies indicate that the low-lying excited structure, particularly the prominent  $0.847(2^+)$  keV level, is

---

Table 4.3.1. Parameters of the ISOM model of the text. Geometrical parameters are given in fermis, energies (E) in MeV, real- and imaginary-potential strengths as volume-integrals-per-nucleon in units of MeV-fm<sup>3</sup>, and the spin-orbit strength in MeV.

---

Real Potential

$$J_v = 506.0 - 6.6837 \cdot E + 0.059882 \cdot E^2$$

$$r_v = 1.300 - 0.0038 \cdot E$$

$$a_v = 0.6338$$

Imaginary Potential

$$J_{ws} = 150.35 - 7.3301 \cdot E \quad (E < 7.5)$$

$$= 95.975 - 0.080151 \cdot E \quad (E \geq 7.5)$$

$$J_{wv} = -16.15 + 1.35 \cdot E \quad (E > 12)$$

$$r_w = 1.260 - 0.0024 \cdot E$$

$$a_w^* \quad C = 0.70 \text{ fm}, \quad D = 12.65 \text{ MeV}$$

Spin-orbit Potential

$$V_{so} = 5.9099 - 0.015 \cdot E$$

$$r_{so} = 1.103$$

$$a_{so} = 0.560$$

---

\*  $a_w \equiv \frac{C \cdot (E - E_F)^2}{(E - E_F)^2 + D^2}$ , where  $E_F$  is the fermi energy = - 9.225 MeV.

---



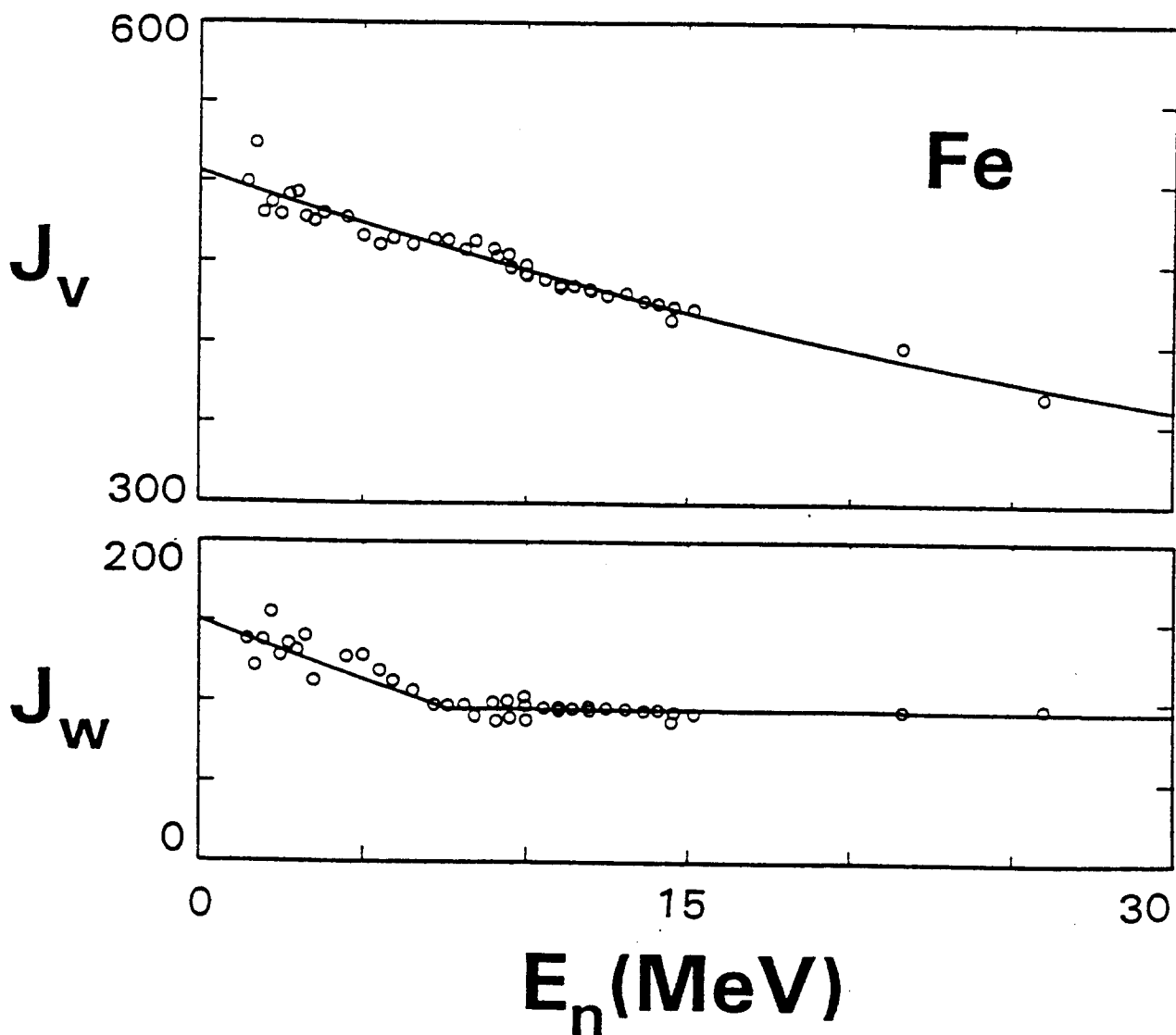


Fig. 4.3.1. The energy dependence of the real,  $J_v$ , and imaginary,  $J_w$ , potential strengths of the ISOM expressed as volume-integrals-per-nucleon in units of  $\text{MeV}\cdot\text{fm}^3$ . The symbols indicate the results of individual fits and curves the parameterizations of Table 4.3.1.

---

Table 4.3.2. Parameters of the ESOM model of the text. Geometrical parameters are given in fermis, energies (E) in MeV, real and imaginary strengths as volume-integrals-per-nucleon in units of MeV-fm<sup>3</sup>, and the spin-orbit strength in MeV.

---

-----

Real Potential

$$J_v = 523.0 - 7.5739 \cdot E + 0.056949 \cdot E^2$$

$$r_v = 1.320 - 0.0052 \cdot E$$

$$a_v = 0.6442$$

Imaginary Potential

$$J_{ws} = 175.0 - 10.6989 \cdot E \quad (E \leq 6.8)$$

$$= 109.8 - 1.1107 \cdot E \quad (E > 6.8)$$

$$J_{wv} = -16.15 + 1.35 \cdot E \quad (E \geq 12)$$

$$r_w = 1.425 - 0.0346 \cdot E \quad (E \leq 5)$$

$$= 1.260 - 0.0016 \cdot E \quad (E > 5)$$

$$a_w^* =, \quad C = 0.75 \text{ fm}, \quad D = 11.58 \text{ MeV}$$

Spin-orbit Potential

$$V_{so} = 5.9099 - 0.015 \cdot E$$

$$r_{so} = 1.103$$

$$a_{so} = 0.560$$

---

\*  $a_w \equiv \frac{C \cdot (E - E_F)^2}{(E - E_F)^2 + D^2}$ , where  $E_F$  is the fermi energy = - 9.225 MeV.

---

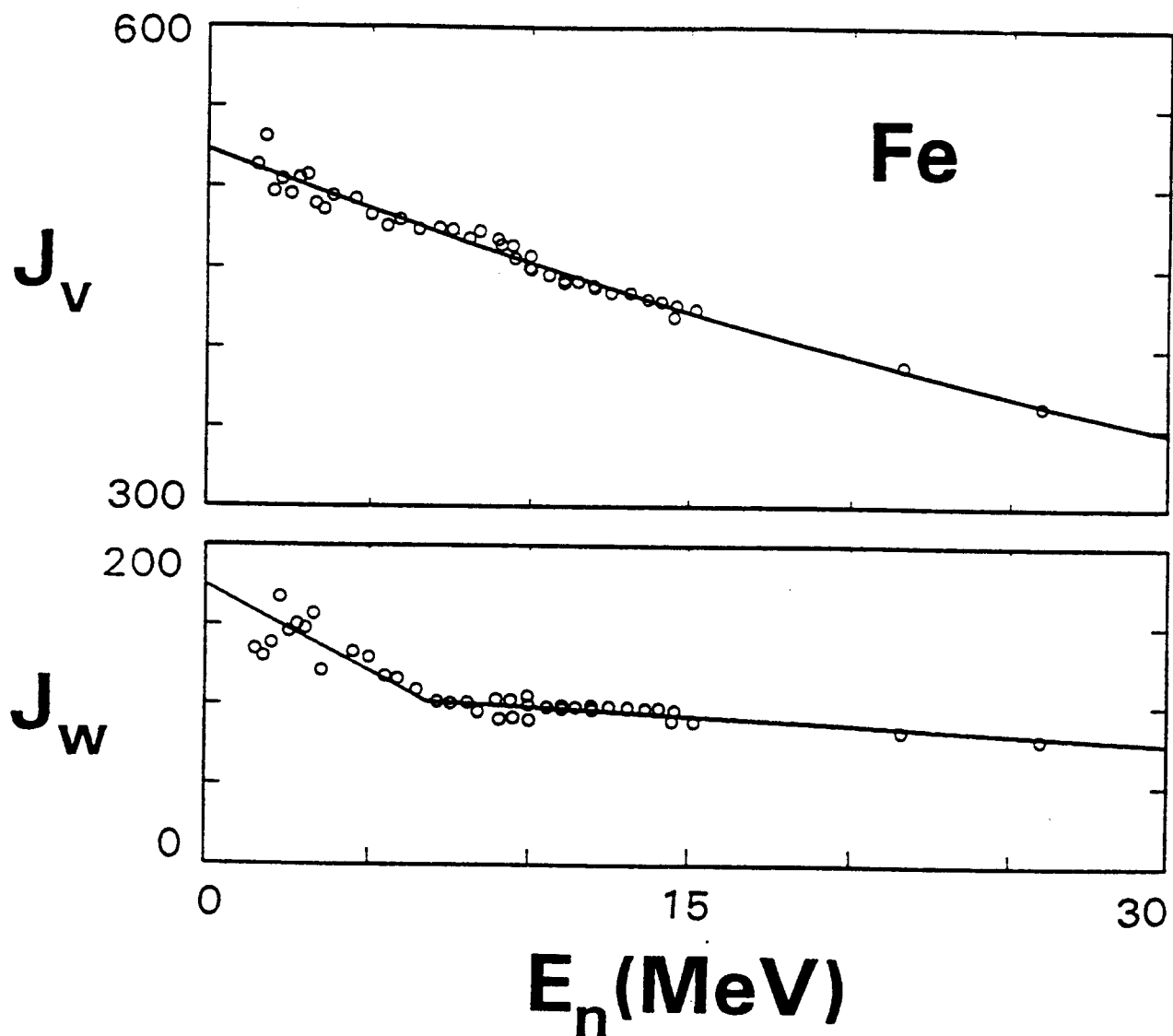


Fig. 4.3.2. Energy dependencies of the real,  $J_v$ , and imaginary,  $J_w$ , potential strengths of the ESOM. The curves reference the parameters of Table 4.3.2, otherwise the nomenclature is the same as for Fig. 4.3.1.

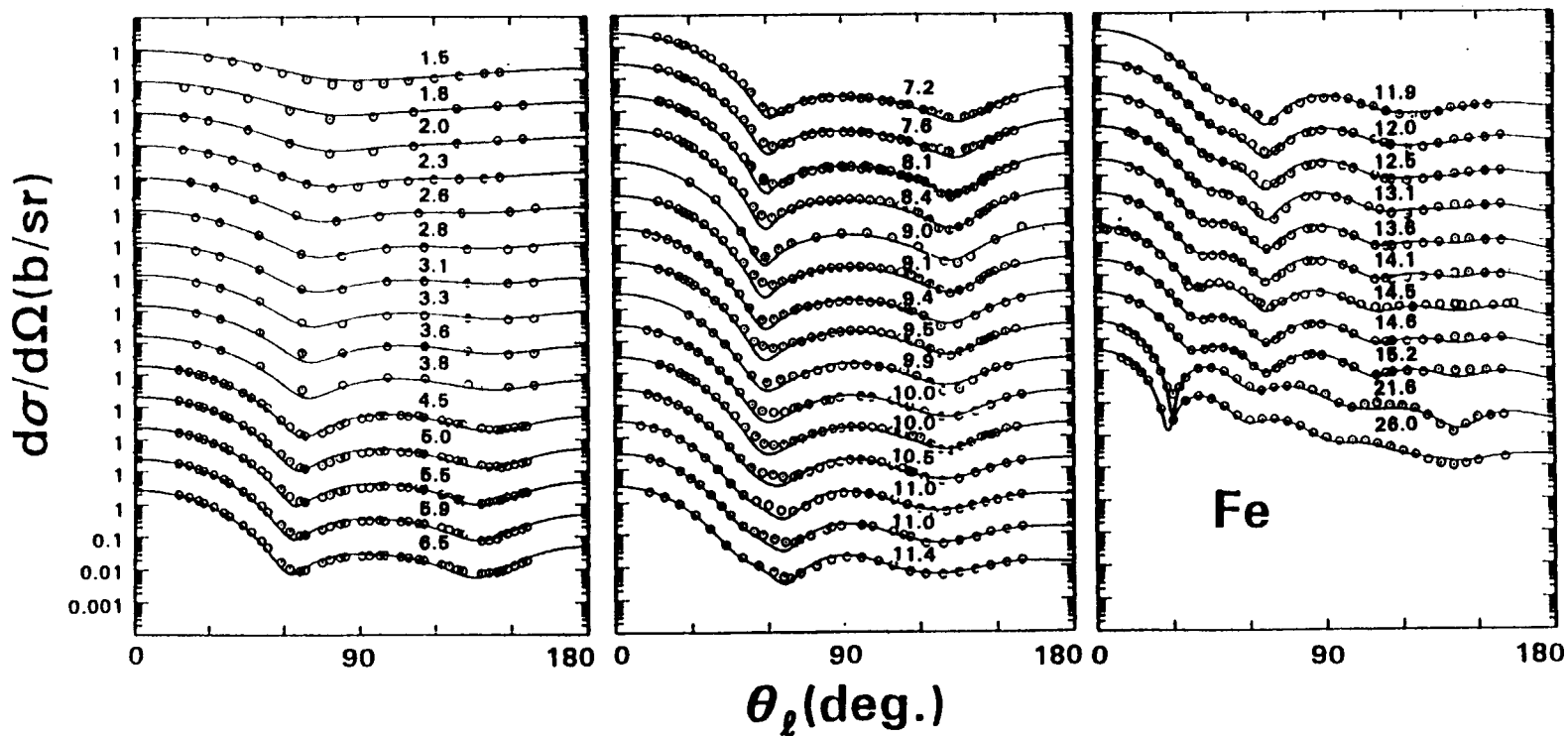


Fig. 4.3.3. Comparison of measured (symbols) and calculated (curves) elastic-scattering cross sections of elemental iron. The calculations employed the ESOM of the text. Approximate incident-neutron energies are numerically noted in MeV.

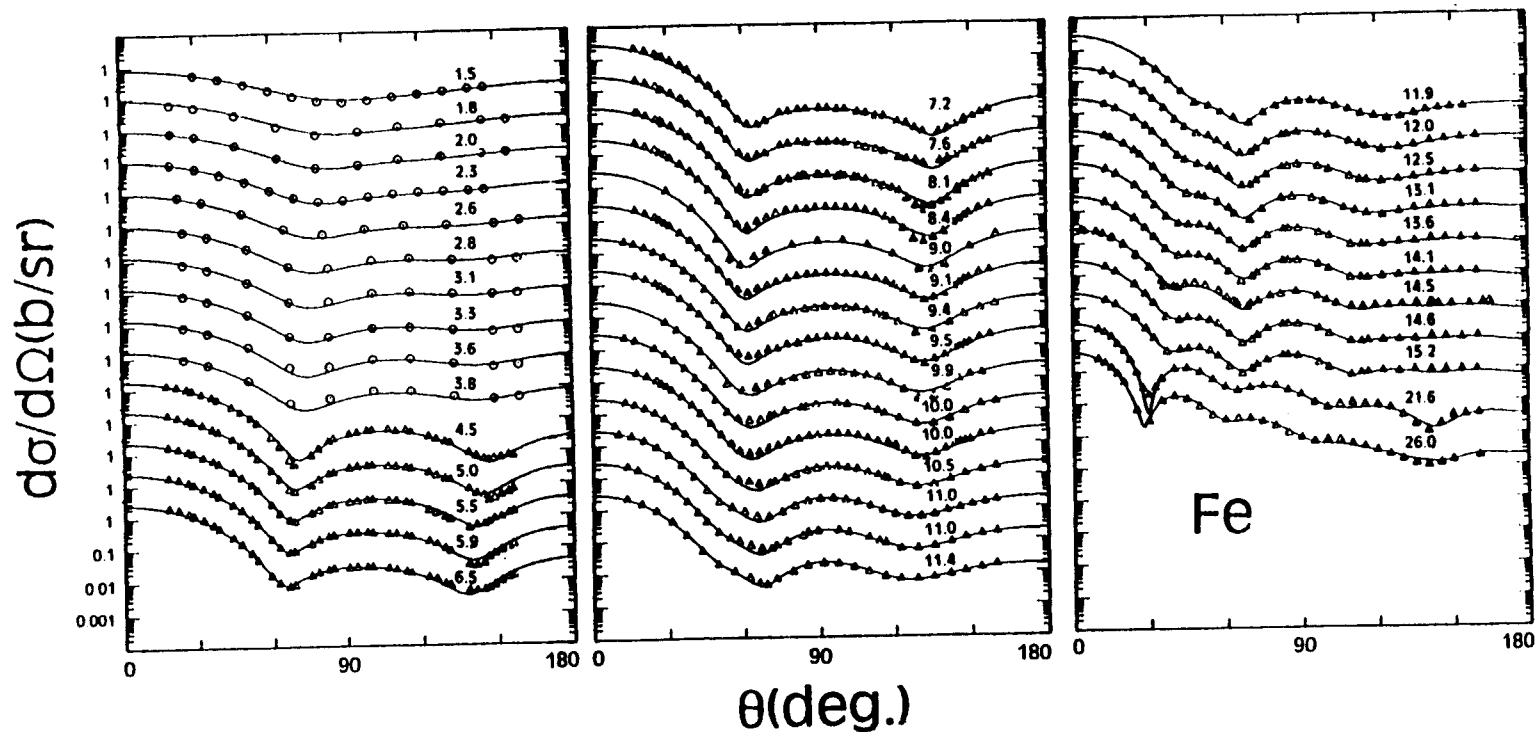


Fig. 4.4.1. The elastic-scattering data base used in the CCM derivations. "o" symbols indicate measured values inclusive of CE contributions. "Δ" symbols indicate experimental results exclusive of CE contributions where the measured values from 4.5 → 10 MeV have been adjusted for CE effects as described in the text. Curves indicate the results calculated with the CCVIB model with  $\beta_2 = 0.239$ . Approximate incident energies are numerically noted in MeV.

characteristic of a relatively hard prolate rotor ([MR79], [LWS81]). In the present considerations of the neutron scattering both alternatives are considered. First it was assumed that neutron scattering from  $^{56}\text{Fe}$  can be represented by a simple one-phonon vibrational model coupling the ground and yrast  $2^+$  levels. Herein this approach is termed the CCVIB model. The second approach assumes that  $^{56}\text{Fe}$  is a rotor with the ground and yrast  $2^+$  levels coupled together. The latter alternative is referred to as the CCROT model. In both approaches, higher-order couplings are ignored. All the coupled-channels calculations employed the calculational code ANLECIS [Mol82A], which is a version of ECIS79 [Ray79].

#### 4.4.1. The vibrational model (CCVIB)

The entire elastic-scattering fitting procedure employed for the SOM was repeated using the vibrational assumptions, the adjusted data base of Fig. 4.4.1, and with the  $\beta_2 = 0.239$  taken from the compilation of Raman et al. [Ram+87]. The resulting potential parameters are given in Table 4.4.1. The energy dependencies of the real,  $J_v$ , and imaginary,  $J_w$ , potential strengths are illustrated in Fig. 4.4.2.  $J_v$  decreases with energy in a manner very similar to that of the ESOM.  $J_w$  decreases with energy for the first few MeV then rises slowly with energy. The results of the CCVIB elastic-scattering calculations are compared with the data base from which it was developed in Fig. 4.4.1. Figure 4.4.3 illustrates similar comparisons between measured and calculated differential cross sections for the excitation of the  $847(2^+)$  keV level, and Fig. 4.1.2 compares measured and calculated neutron total cross sections. The volume absorption of the ESOM was not in evidence with the CCVIB.

#### 4.4.2. The rotational model (CCROT)

The fitting employed for the CCVIB, above, was repeated using the rotational coupling scheme and the same  $\beta_2 = 0.239$ . The resulting potential parameters are given in Table 4.4.2, and the energy dependencies of the real- and imaginary-potential strengths are shown in Fig. 4.4.4. The measured differential elastic-scattering cross sections of the relevant data base are compared with the CCROT calculated results in Fig. 4.4.5. Similar comparisons for the excitation of the  $847(2^+)$  keV are shown in Fig. 4.4.6, and of measured and calculated neutron total cross sections in Fig. 4.1.2.

---

Table 4.4.1. Parameters of the CCVIB ( $\beta_2 = 0.239$ ) model of the text. Geometrical parameters are given in fermis, energies (E) in MeV, real and imaginary strengths as volume-integrals-per-nucleon in units of MeV-fm<sup>3</sup>, and the spin-orbit strength in MeV.

-----

Real Potential

$$\begin{aligned}J_v &= 540.0 - 7.030 \cdot E \\r_v &= 1.3752 - 0.007962 \cdot E \\a_v &= 0.6538\end{aligned}$$

Imaginary Potential

$$\begin{aligned}J_w &= 115.0 - 5.1500 \cdot E \quad (E < 7.5) \\&= 73.156 + 0.42922 \cdot E \quad (E \geq 7.5) \\r_w &= 1.3675 - 0.007934 \cdot E \\a_w &= 0.21515 + 0.018297 \cdot E\end{aligned}$$

Spin-orbit Potential

$$\begin{aligned}V_{so} &= 5.9099 - 0.015 \cdot E \\r_{so} &= 1.103 \\a_{so} &= 0.560\end{aligned}$$

---

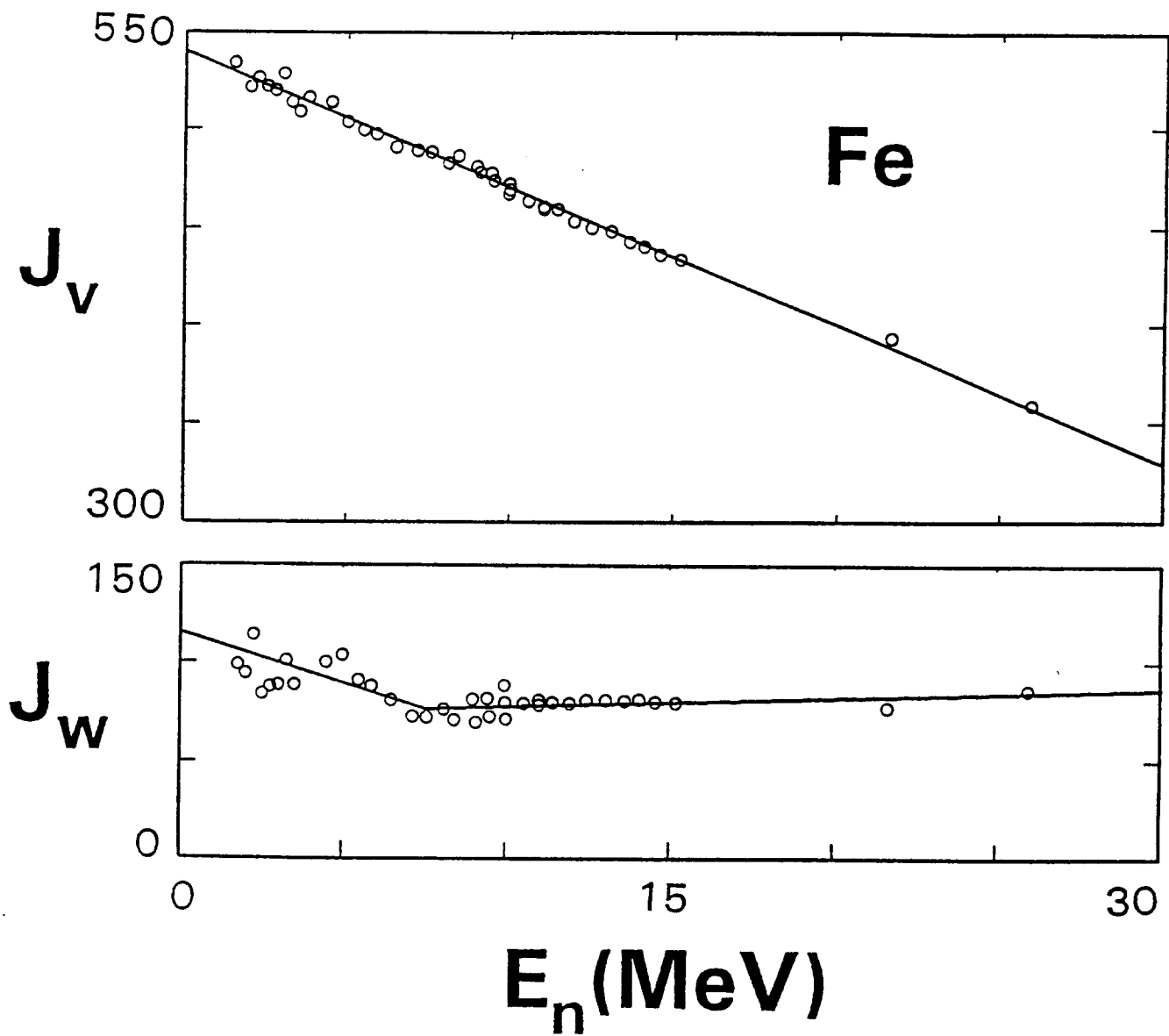


Fig. 4.4.2. Energy dependencies of the real,  $J_v$ , and imaginary,  $J_w$ , strengths of the CCVIB. The nomenclature is the same as in Fig. 4.3.1 except that the curves are referenced to Table 4.4.1.



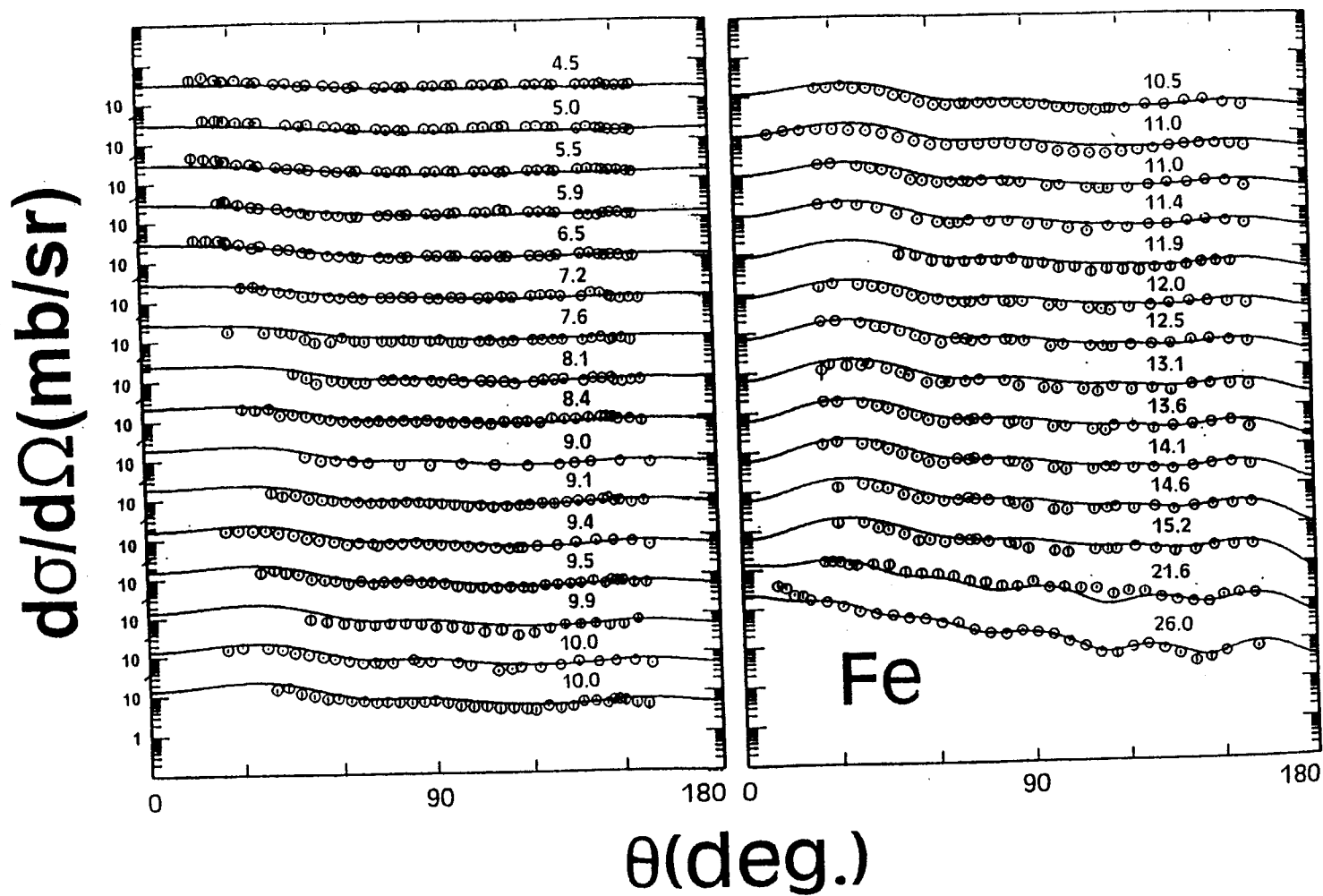


Fig. 4.4.3. Comparison of measured differential cross sections for the excitation of the iron 847 keV level (symbols) with the results of CCVIB calculations (curves). Incident energies are numerically noted in MeV.

---

Table 4.4.2. Parameters of the CCR0T ( $\beta_2 = 0.239$ ) model of the text. Geometrical parameters are given in fermis, energies (E) in MeV, real and imaginary strengths as volume-integrals-per-nucleon in units of MeV-fm<sup>3</sup>, and the spin-orbit strength in MeV.

---

-----

Real Potential

$$\begin{aligned} J_v &= 535.5 - 5.842 \cdot E \\ r_v &= 1.3315 - 0.005753 \cdot E \\ a_v &= 0.6603 \end{aligned}$$

Imaginary Potential

$$\begin{aligned} J_w &= 115.0 - 5.0958 \cdot E \quad (E < 7.5) \\ &= 70.404 + 0.85026 \cdot E \quad (E \geq 7.5) \\ r_w &= 1.3472 - 0.0049424 \cdot E \\ a_w &= 0.21166 + 0.012819 \cdot E \end{aligned}$$

Spin-orbit Potential

$$\begin{aligned} V_{so} &= 5.9099 - 0.015 \cdot E \\ r_{so} &= 1.103 \\ a_{so} &= 0.560 \end{aligned}$$


---

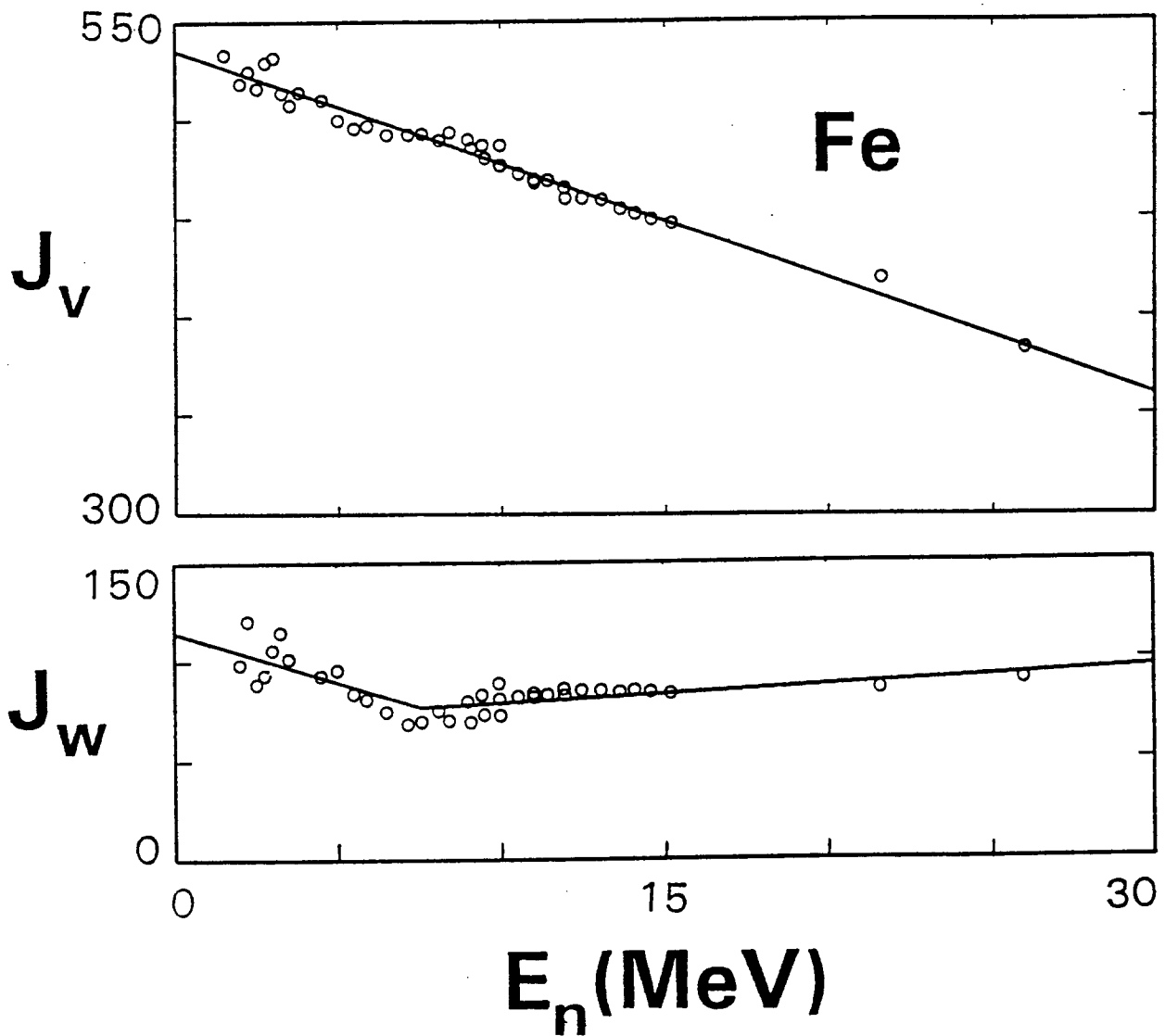


Fig. 4.4.4. Energy dependencies of the real,  $J_v$ , and imaginary,  $J_w$ , potential strengths of the CCROT expressed in terms of volume-integrals-per-nucleon. The nomenclature is the same as Fig. 4.3.1 except the curves are referenced to Table 4.4.2.

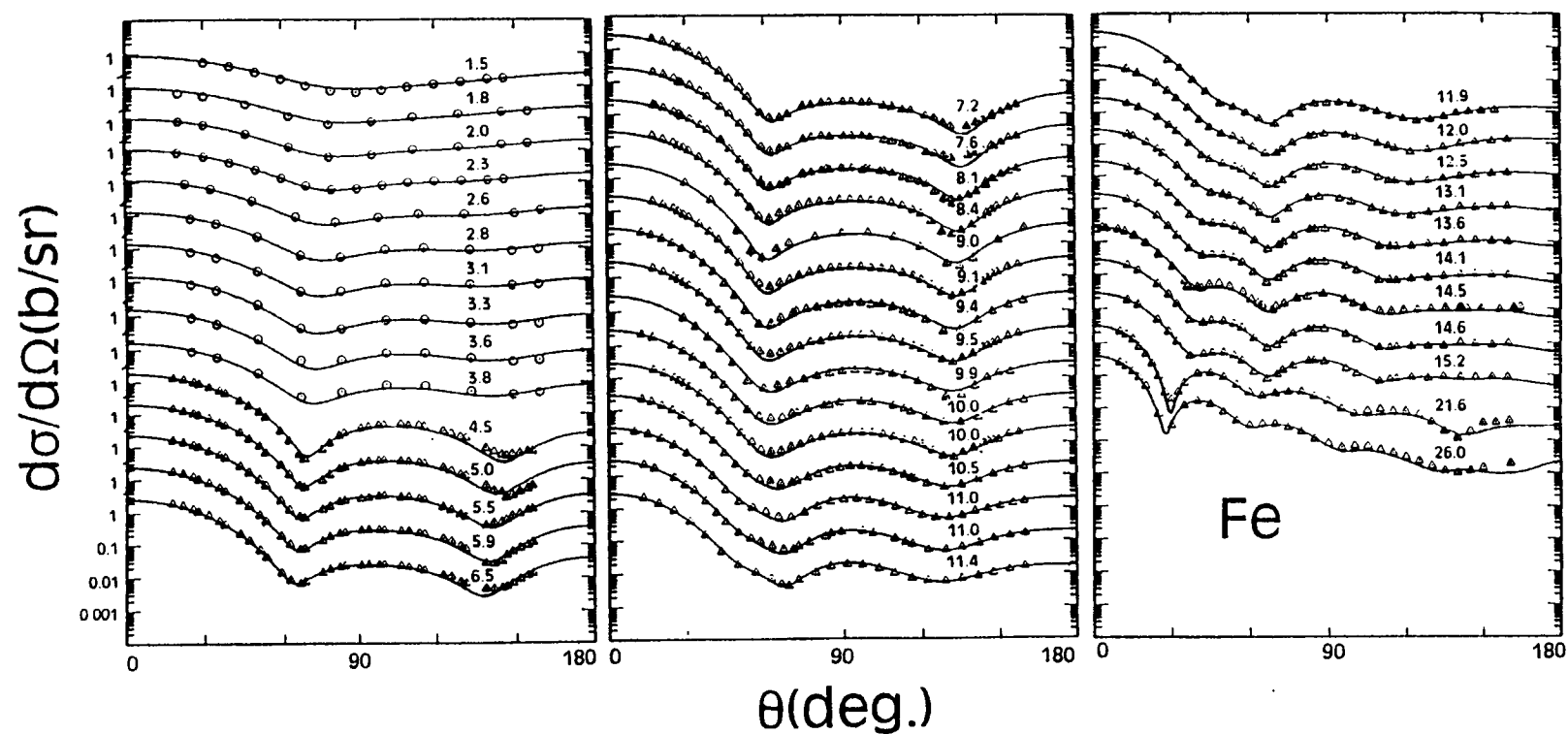


Fig. 4.4.5. Comparison of experimentally derived (symbols) and calculate (curves) differential elastic-scattering cross sections. The calculations employed the CCROT potential, and the nomenclature is the same as Fig. 4.4.1.

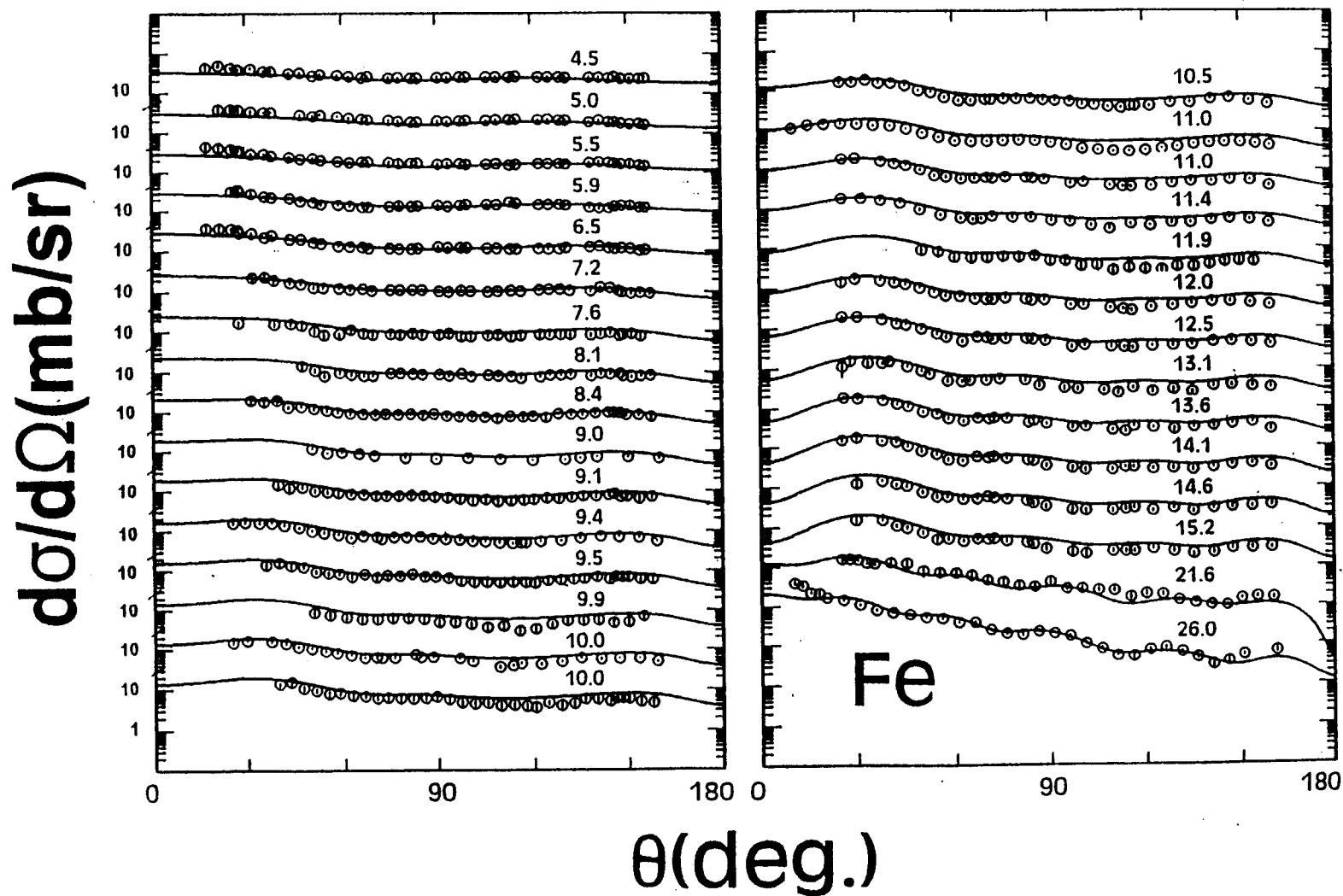


Fig. 4.4.6. Comparison of measured differential cross sections for the excitation of the iron 847 keV state (symbols) with the results of CCR0T calculations (curves). The notation is the same as for Fig. 4.4.3.

## 5. DISCUSSION AND SUMMARY

### 5.1. Comparison of the ISOM, ESOM, CCVIB and CCROT potentials

These four potentials were deduced over many months. They have a commonality in the data base, the spin-orbit potential and the fitting methodology, but otherwise are independent. All the real-potential diffusenesses,  $a_v$ , are energy independent, with those of the SOM's being somewhat small than for the CCM's. This is expected when SOM's are applied to collective vibrators or rotors, as illustrated in Appendix B. The real-potential radii,  $r_v$ , all decrease with energy, somewhat more sharply in the CCVIB case. All are of about the same magnitude at  $\approx 15$  MeV. Theoretical predictions suggest that the real-potential rms radius,  $\langle R^2 \rangle^{1/2}$ , of SOM's should very slowly decrease with energy [JLM77]. This differs from the present results where the  $\langle R^2 \rangle^{1/2}$  of the ESOM (and ISOM) decreases by  $\approx 6\%$  over the  $\approx 0 - 26$  MeV range of the data base used in the present work. This trend is consistent with the dispersion contribution which augments the Saxon-Woods real potential with a surface component that decreases with energy and becomes very small at high energies, as discussed in Section 5.12. Thus, the  $\langle R^2 \rangle^{1/2}$  of the ESOM at 21.6 MeV is  $\approx 4.31$  fm which agrees with the result implied by the potential of ref. [Ols+87], and at 26 MeV the ESOM value is  $\approx 4.20$  fm compared with the 4.253 fm value resulting from the work of ref. [Mel+83]. Systematics of SOM's suggest a  $r_v = 1.2604$  fm at 8 MeV [Chi+90] which is only  $\approx 1.15\%$  smaller than the present SOM results. The real-potential strengths,  $J_v$ , have approximately the same energy dependencies, which are qualitatively characteristic of the predictions of local-equivalent Hartree-Fock calculations though of significantly larger slope, as has been reported elsewhere [AY80]. A part of this energy dependence can be attributed to dispersive effects (see Section 5.12). The normalizations of the  $J_v$  values are different with those of the SOM's generally 2 - 4% smaller than for the CCM's over the large majority of the relevant energy range. Such a trend is expected from the use of the SOM to describe the neutron interaction with a collective target (see Appendix B). Systematics of SOM's predict a  $J_v = 453 \text{ MeV-fm}^3$  at 8 MeV [Chi+90] which is only  $\approx 1.7\%$  smaller than the present results.

All of the imaginary-potential strengths,  $J_w$ , linearly decrease from quite large values at zero energy to  $\approx 7$  MeV. This common characteristic results in relatively small total cross sections over the fluctuating low-energy region. The  $J_w$  values of the SOM's are generally larger than those of the CCM's due to the explicit treatment of the yrast ( $2^+$ ) level in the latter. Above  $\approx 7$  MeV the  $J_w$  of the SOM's are constant or slowly decrease with energy, contrary to what

one would expect as more channels open. In contrast the  $J_w$ 's of the CCM's somewhat increase with energy over the same energy range, although not as rapidly as one might expect. The behavior of the  $J_w$  values is influenced by the dispersion relationship, as discussed in Section 5.11. In addition, the use of the SOM to represent collective nuclei can lead to large differences in  $J_w$  values, as illustrated in Appendix B. All of the imaginary-potential radii,  $r_w$ , are energy dependent. Those of the SOM's are considerably smaller than  $r_v$ , while for the CCM's  $r_w \approx r_v$ . Again, this may well reflect the use of the SOM for treating collective nuclei (see Appendix B). The  $r_w$  is also sensitive to dispersion effects as discussed in Section 5.12. The formulation of the energy dependence of imaginary-potential diffuseness,  $a_w$ , is different for the SOM's and CCM's. However, in all cases  $a_w$  is small (or zero) at the Fermi Energy, as has been previously observed [Smi94], and rapidly increases with energy. Given the different formulations, the  $a_w$  of the present SOM's and CCM's are relatively consistent.

There is a difference between SOM and CCM potentials due to absence of the volume-imaginary potential in the latter cases. At higher energies, volume absorption must occur but where it becomes significant and how it is introduced is a matter of some debate. In the SOM potentials of Section 4 it is represented as a small linear contribution starting at 12 MeV. In the CCM derivations no clear evidence of volume absorption could be identified. This is consistent with the results of ref. [Del+82] where those authors concluded that, in the region of the present study, it may be an artifact of using a SOM to represent the neutron interaction with a collective target. Some global models introduce volume absorption at  $\approx 15$  MeV (e.g., [RKF79]) and others consider it at very low energies (e.g., [Ped+88]). The present neutron elastic-scattering data base contains only two elastic-scattering distributions at energies above  $\approx 15$  MeV (at 21.6 and 26 MeV), and that is not a good foundation for definitive determination of possible contributions from volume absorption. Moreover, the authors of the 21.6 results [Ols+87] concluded that the volume absorption was not present in their SOM interpretation of neutron scattering from iron. Neutron total cross sections, which extend over a wide energy range, are not particularly sensitive to small volume-absorption effects. Theoretical considerations [JLM77] suggest that volume absorption becomes predominant only at  $\approx 50$  MeV.

All of the present potentials are explicitly relevant only to the energy range of the data base (i.e.,  $0 \rightarrow 26$  MeV). Quite clearly, some of the parameter energy dependencies can not continue indefinitely, and must asymptotically approach some constant values at or above 26 MeV. Some of these high-energy trends are described in ref. [Ped+88].

## 5.2. Comparisons of phenomenological potentials

There are a few detailed studies in the literature of neutron scattering from elemental iron or  $^{56}\text{Fe}$  at energies of  $\approx > 8$  MeV from which phenomenological optical or coupled-channels models were deduced. El-Kadi et al. [ElK+82] measured elastic scattering from  $^{56}\text{Fe}$  at 8, 10, 12 and 14 MeV, and derived a conventional SOM. The same data was re-interpreted by Delaroche et al. [Del+82] to obtain a vibrational CCM. Ferrer et al. [Fer+77] measured elastic scattering from elemental iron at 11 MeV and deduced a SOM. Similar work was done by Hansen et al. [Han+84] at 14.6 MeV. Mellema et al. [Mel+83] measured elastic scattering from  $^{56}\text{Fe}$  at 20 and 26 MeV and deduced SOM's. Olsson et al. [Ols+87] studied elastic scattering from a number of targets, including elemental iron, at 21.6 MeV and deduced SOM's.

There are differences in the real potentials resulting from the above endeavors. For example, the real radii tend to fall into two classes; for one group  $r_v$  is quite small (e.g.,  $\approx 1.19$  fm), and considerably larger (e.g.,  $\approx 1.29$  fm) for the other. In one instance, data sets from the same institution lead to alternate choices of  $r_v$ . The present  $J_v$ 's are reasonably consistent with previous results reported in the literature. Exceptions are the potentials of refs. [ElK+82] and [Del+82] where the  $J_v$ 's are notably smaller and have less energy dependence. Both of these references are based upon the same experimental data. However, most of that experimental data was included in the present interpretations and the results of the fitting were not notably different from those obtained from the body of the data base. There is considerable variation in the volume-imaginary potential strength. In some cases it is significant at quite low energies while in others it is non-existent. Given the uncertainties in volume absorption, the  $J_w$ 's are similar to one another and to those deduced in the present work. This is particularly so if one compares total imaginary strengths.

The present work attempts to determine the phenomenological potentials for neutron scattering from iron from very low energies to  $> 25$  MeV. In doing so the energy dependencies of the model parameters are much better defined than in previous work at isolated or few incident energies. For example, the present work suggests that  $r_v$  decreases with energy and thus is consistent with the smaller values reported at higher energies (e.g., at 20  $\rightarrow$  25 MeV) and with the larger values reported in some of the lower-energy work [Fer+77]. It is also noted that the majority of the results in the literature, and the present work, suggest an energy dependence of  $J_v$  in excess of that predicted by local-equivalent Hartree-Fock calculations or as commonly encountered in "global" models. Such a behavior is consistent with appreciable dispersion contributions to the real potential over the



energy range of the present work, as discussed in Section 5.12.

There have been a number of "global" neutron optical potentials reported in the literature (e.g., see the compilation of ref. [You86]). They generally fall into two classes. The first of these is based upon low-energy (below several MeV) data and describes the observables in that energy region quite well, but fails to characterize them at higher energies (e.g., above 10 MeV). These low-energy potentials generally have rather large radii. A representative example is the model of Moldauer [Mol63]. The second category of "global" potentials is based upon higher-energy data and describes the observables in that region quite well. The real-potential radii are generally quite small (e.g., 1.2 fm or less). Examples of the second category are the "global" potentials of refs. [RKF79] and [Ped+88]. Such potentials become increasingly unsuited to  $^{56}\text{Fe}$  as the energy falls below  $\approx 10$  MeV (e.g., yield total cross sections at  $\approx 2$  MeV that are 10 - 20% larger than the average of the measured values). This shortcoming was recognized in ref. [Ped+88] where it was suggested that the real-potential strength should increase rather rapidly by up to 5 - 10% as the energy falls below  $\approx 5$  MeV, though the quantitative behavior was not explored. This dichotomy between low- and high-energy potentials is removed in the present interpretations where the real-potentials are quite similar to those of the high-energy "global" models at 20 MeV, have somewhat larger strengths at 10 MeV, and much larger strengths and radii at a few MeV where they become similar to those of the low-energy models.

### 5.3. Equation of state

The real mean-field potential, often called the "equation of state", is generally derived from bound-state and proton-scattering data over a wide energy range; e.g., from  $\approx -200$  MeV to  $+200$  MeV. In these derivations data in the  $\approx -20$  to  $+20$  MeV region are usually ignored as the behavior of the potential may be distorted by dispersion effects [Sat83]. Illustrative of such considerations is the work of Bauer et al. [Bau+82]. Those authors proposed a real-potential strength of  $J_v \approx 475.2 - 3.34 \cdot E$  for neutrons incident

on  $^{56}\text{Fe}$  (a linear representation of the results of ref. [Bau+82] is used as it is a good approximation over the energy range of the present work). The energy dependence is significantly less than those of the present potentials. The latter all have much larger strengths at  $E = 0$ , but at  $\approx 25$  MeV are very similar to the general parameterization of ref. [Bau+82]. The strong energy dependence of the present potentials is not unique, as cited above.

### 5.4. Total cross sections

The potentials of Section 4 imply neutron total cross sections that are similar to one another and to the experimental results of refs [Cie+68] and [Lar80], as illustrated in Fig. 4.1.2. All of the potentials have large  $J_w$ 's at low energies. This characteristic leads to smaller total cross sections below several MeV, as indicated by the

measurements. A simple extrapolation of the high-energy portion of the potentials to low energies does not give such a behavior. However, the exact nature of these low-energy trends of the potentials or the measured values is obscured by large fluctuations of a statistical nature, or by the presence of doorway configurations [EM69]. Of the SOM's, the ESOM gives the best description of the measured values over the  $< 8$  MeV region but is less suitable at higher energies. The CCVIB and CCR0T results differ by small amounts at lower energies. Due to the fluctuations, the experimental results offer little guidance as to the choice between the two. However, taken over the full range of the experimental data, the CCM's give a better representation of the measured data than those based upon SOM's. Either collective model results in total cross sections above several MeV that agree with the measured values to within the order of 1%, and the experimental results from different sources differ by about the same amount. This good agreement between measured and calculated total cross sections suggests that the elastic-scattering data base, primarily used in the model derivations, is correctly normalized.

### 5.5. Differential elastic scattering

As elemental iron is dominated by the isotope  $^{56}\text{Fe}$  it is not surprising that the ISOM and ESOM potentials are similar and that they give essentially the same description of the data base from which they were primarily derived (compare Figs. 4.3.3 and 4.1.1, respectively). Both descriptions are quite good, with discrepancies that are often of the same order as those between experimental data sets from different institutions. However, there are some systematic problems, notably about 10 MeV where the calculated results give cross sections near the first minimum of the distributions significantly below the measured values. This is a region that is sensitive to multiple-scattering corrections to the experimental data but the discrepancies are larger than one might expect from such a source, and at least two of the experimental data sets gave very careful attention to the corrections using independent methods and with consistent results. The other region of possible systematic discrepancy is at the very highest energies and large scattering angles where the ESOM appears to give results superior to those obtained with the ISOM. These differences may well be only an artifact of the fitting procedures as the discrepancies are relatively small and confined to the highest several energies of the data base.

The CCM models give an improved description of the elastic-scatter data from which they were developed, as illustrated in Figs. 4.4.1 and 4.4.5. In particular, the minima of the distributions near 10 MeV are better represented than with SOM's. The CCVIB and CCR0T elastic-scattering results are very similar with the biggest differences at the large scattering angles and very highest energies of the data base. In that limited region, perhaps the CCVIB model provides an arguably better description of the experimental results. Whether this is a reflection of the reaction mechanism or simply a result of small fluctuations in the fitting procedures is uncertain.

Such a behavior is not evident in the independent interpretations of the highly accurate PTB data [Sch94], as discussed in Appendix A.

Generally, the elastic-scattering data supports the choice of CCM's over SOM's but offers little, if any, guidance as to the selection of CCVIB or CCR0T models.

### 5.6. Differential inelastic scattering

Of course, the simple spherical models simply do not account for the inelastic-neutron excitation of the yrast  $847(2^+)$  state as they make no provision for the significant direct excitation. They do give a reasonable description of the excitation of the higher-lying levels where the cross sections are largely of a CN nature (see Fig. 3.2.2). The angle-integrated cross sections for the excitation of the yrast  $2^+$  state calculated with the CCVIB and CCR0T models are essentially indistinguishable, as illustrated in Fig. 3.2.3. At higher energies they tend to be slightly larger than the measured values though there are exceptions, notably at 21.6 MeV where the calculated values are a bit lower than the measured quantities. These modest discrepancies can be alleviated with variations in  $\beta_2$  or modifications of the coupling schemes; however, these approaches were not attempted due to the variations in the data from various institutions. The magnitude trends are evident in comparisons of measured and calculated inelastic differential distributions shown in Figs. 4.4.3 and 4.4.6. These two figures also indicate that the calculated results are bit lower than the measured values at very forward angles at the lowest and highest energies of the data base. These discrepancies are probably of an experimental origin as resolutions deteriorate at the lowest energies of the present measurements due to target thickness and at the very highest energies of the literature values the experimental velocity resolution is marginal. The angular distributions calculated with the CCVIB and CCR0T models significantly differ only at very forward and very back angles where there is no experimental data upon which to base a selection. Where there is data the differences in shape are so small that a selection between the two models is difficult. Thus the inelastic-scattering angular distributions provide little guidance as to the choice of CCM models. The same is true for the angle-integrated inelastic-scattering cross sections, as illustrated in Figs. 3.2.2 and 3.2.3.

### 5.7. Strength functions

It is common practice to test neutron models by comparing measured and calculated s- and p-wave strength functions. Such comparisons are less rewarding in the present case as there are large cross-section fluctuations at lower energies, some of which may be associated with doorway states [EM69]. As a consequence, experimentally-deduced strength functions may represent a local phenomena not characteristic of the general trends described by the energy-averaged models. With this caveat, strength functions were calculated and compared with those deduced from measurements, with the

results given in Table 5.7.1. The calculated s-wave strength functions tend to be somewhat larger than those deduced from measurements. The calculated p-wave strength functions are a factor of two or more larger than deduced from experiment, and this is well beyond the uncertainty attributed to the experimentally-based values. The calculated strength functions are very sensitive to the details of the low-energy behavior of the respective potentials which are somewhat uncertain due to the large energy-dependent fluctuations at low energies.  $^{56}\text{Fe}$  lies near the peak of the s-wave strength function and the minimum of the p-wave strength function. It is a region where energy-averaged models have difficulties representing  $l = 0$  and  $l = 1$  strength functions (see ref. [You86] for examples).

### 5.8. Scattered-neutron polarizations

Surprisingly, there appear to be no comprehensive elastic-scattering polarization measurements for  $^{56}\text{Fe}$  or elemental iron at sufficiently high energies to avoid fluctuating contributions from CN processes. There have been a number of  $^{54}\text{Fe}$  polarization studies at incident energies of  $\approx > 10$  MeV. The present models were extrapolated to that isotope and used to calculate scattered-neutron polarizations. The extrapolation involved the common size effect, small corrects for the difference in nuclear asymmetry, and corrections for changes in deformation; i.e., changes in  $\beta_2$ . The size effect follows from  $R = r \cdot A^{1/3}$ . Asymmetry corrections were made using the constants discussed in Section 5.10, and  $\beta_2$  of  $^{54}\text{Fe}$  was taken to be 0.195 as given in ref. [Ram+87]. With these small adjustments, the polarization of 13.9 MeV neutrons elastically-scattered from  $^{54}\text{Fe}$  was calculated using ESOM, CCVIB and CCROT models. The results are compared with the measured values of Floyd et al. [Flo+83] in Fig. 5.8.1. The agreement between measured and calculated values is reasonably good, approaching that obtained in detailed studies of polarization effects [Flo+83]. This is rather remarkable as a non-deformed spin orbit-potential was used in the present work and the detailed  $^{54}\text{Fe}$  polarization studies of ref. [Flo+83] suggest that the spin-orbit potential is deformed and very possibly more so than the central Saxon-Woods potential. It should again be noted that shell-model considerations [MR79] indicate that  $^{54}\text{Fe}$  is a vibrational nucleus, in contrast to the rotational character of  $^{56}\text{Fe}$ . This difference has only a small effect on the calculated polarizations, as illustrated in Fig. 5.8.1, and thus polarization comparisons offer little guidance as to the choice of CCVIB or CCROT models.

---

Table 5.7.1. Comparisons of  $^{56}\text{Fe}$  strength functions (in units of  $10^{-4}$ ).

---



---

Source	s-wave	p-wave
ISOM	4.95	1.37
ESOM	2.49	0.83
CCVIB	3.48	0.90
CCR0T	3.97	1.25
EXP. <sup>a</sup>	2.60±0.60	0.45±0.05

---

<sup>a</sup> As given in the compilation of ref. [Mug+82].

---

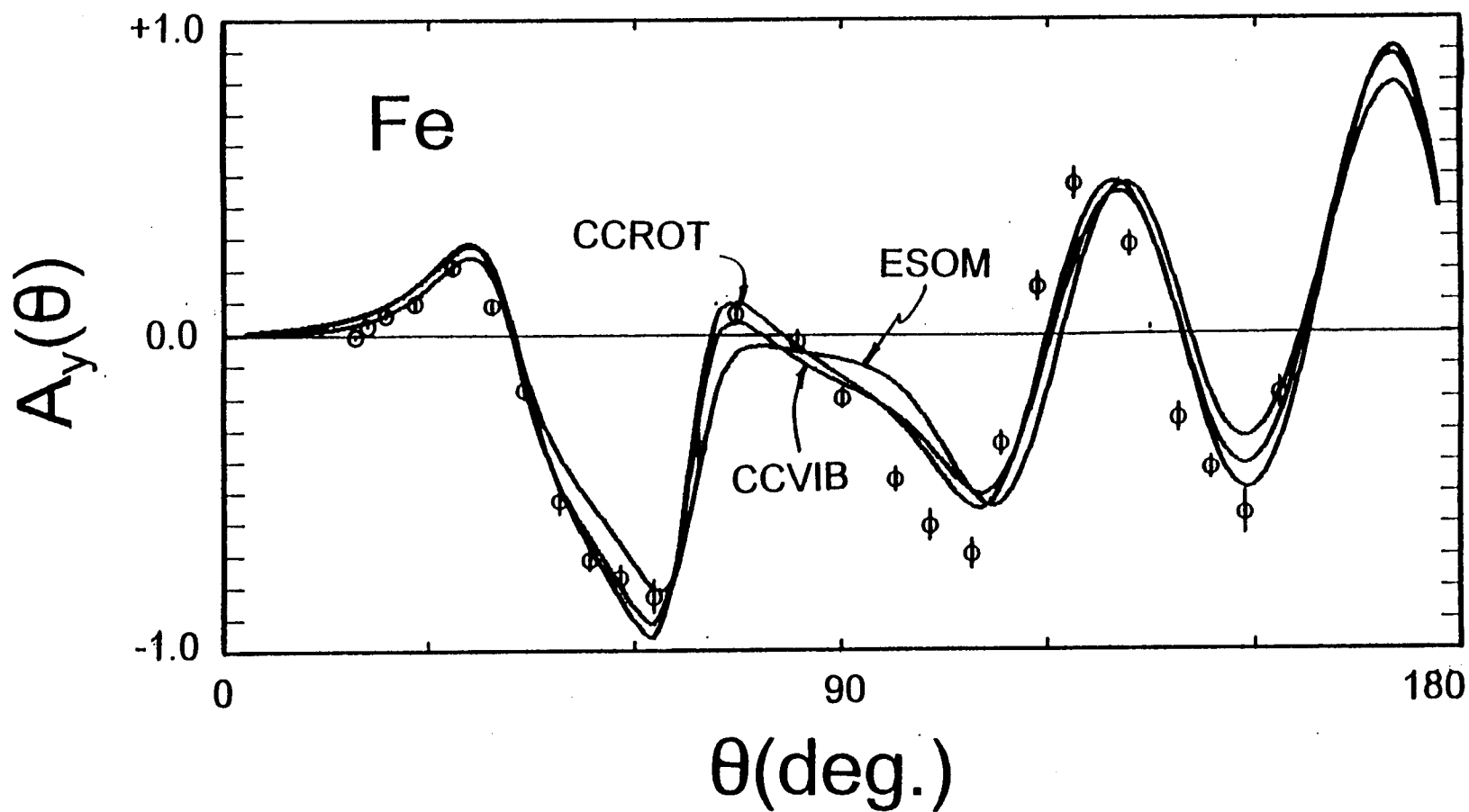


Fig. 5.8.1. Comparison of measured (symbols) and calculated (curves) elastic-scattering polarizations of  $^{54}\text{Fe}$  at an incident energy of 13.9 MeV. The measured data was taken from ref. [Flo+83]. The curves indicate CCROT, CCVIB and ESOM calculated results, respectively.

### 5.9. Deformation and coupling

The two primary isotopes of iron are either at the closed neutron shell of  $N = 28$  ( $^{54}\text{Fe}$ ) or two neutrons above it ( $^{56}\text{Fe}$ , in this Section it is assumed that elemental iron consists entirely of  $^{56}\text{Fe}$ ). One might expect behavior reasonably consistent with the core-coupling model of Madsen, Brown and Anderson [MBA75]. That concept predicts collective behavior due to proton vibrations (or rotations) with a  $\beta_2$  for the neutron interaction ( $\beta_{nn}$ ) larger than that for the proton interaction ( $\beta_{pp}$ ), although in the rotational case strong coupling may somewhat mask the effect [Bai78].

The above phenomenological interpretations assumed a  $\beta_2$  equal to that deduced from coulomb-excitation studies ( $\beta_{em}$ ) [Ram+87]. Examination of other choices of  $\beta_2$  in the context of the full scope of the data base is so tedious as to be impractical. However, detailed examinations of  $\beta_2$  were carried out using the PTB portion of the data base. That set of data is of reasonable energy scope ( $\approx 9.5 \rightarrow 15$  MeV) and detail, may well be the most accurate portion of the overall data base, has the best uncertainty specification, and covers an energy range that is at once reasonably free of compound-nucleus contributions and of uncertainties due to possible volume-absorption contributions. Using the geometries and spin-orbit potential of Table 4.4.2, the PTB data was fitted assuming the rotational model (CCROT), varying real- and imaginary-potential strengths and the deformation  $\beta_2$ . The minimum of  $\chi^2$  as a function of  $\beta_2$  was reasonably well defined despite the strong correlation between  $\beta_2$  and the imaginary strength [Lac+76]. The average value of the  $\beta_2$  resulting from the fitting of the elemental PTB distributions was 0.247, or very similar to that assumed in the above phenomenological interpretations. The  $\beta_2$  values resulting from the fitting decreased by  $\approx 10\%$  over the  $9 \rightarrow 15$  MeV energy range. A similar, but much weaker, energy dependence has been noted in (p,p) studies [Hin+73]. The effect may well be due to the simplicity of the model which ignores such matters as multiple excitation processes. The strength of the interaction is dependent on the potential radius,  $R$ . There is some uncertainty as to what  $R$  should be, particularly as to the inclusion of a contribution from the imaginary potential [Bai+78], but here the conventional assumption of  $R$  equal to the real-potential radius,  $R_v$ , is used. Comparisons should be formulated in terms of the deformation length  $\delta = \beta_2 \cdot R_v$  [Bla63] since it is proportional to the transition amplitude. In this formulation, the present results lead to an average  $\delta_{nn} = 1.192$  fm; with, as for  $\beta_2$ , about a 10% decrease with energy over the energy range of the fitting. The average value is  $\approx 10\%$  larger than the  $\delta_{pp}$

deduced from similar-energy proton-scattering measurements in ref. [Del+82]. The comparison is qualitatively consistent with the predictions of ref. [MBA75] and with the general trends reported in the  $N = 50$  region [Bai+78]. It is not consistent with the comparisons of ref. [Del+82] where  $\beta_{pp} \approx \beta_{nn}$ , although in the latter work unusually small  $R_v$  values were used. The  $\delta_{em}$  value ranges from  $\approx 1.10$  to  $1.12$  fm depending upon the source of  $\beta_{em}$  results (e.g., [Ram+87], [LWS81]). Thus the present  $\delta_{nn}$  value is somewhat larger than  $\delta_{em}$ , contrary to the predictions of the core-coupling model. Whether this is significant or not is uncertain due to the afore-mentioned energy dependencies of  $\beta_{nn}$  and of the geometric parameters used in the present fitting. It is difficult to estimate the uncertainties in the above  $\beta$  values, but they probably are in the range of  $3 \rightarrow 5\%$ .

The above fitting exercise was repeated using the CCVIB model with similar results. The  $\beta_{nn}$  was slightly larger than obtained with the assumption of the CCROT model and was essentially constant over the energy range of the relevant data base. However, the scatter of the individual  $\beta_{nn}$  values was larger as the  $\chi^2$  minimum as a function of  $\beta_2$  obtained in the fitting was not as well defined as with the CCROT. This may suggest that the rotational model is the more realistic.

#### 5.10. Asymmetry

The present work is essentially confined to the neutron interaction with a single target,  $^{56}\text{Fe}$ . Therefore, it does not directly give information as to the asymmetry ( $\eta = (N-Z)/A$ ) dependence of the potentials. However, some indication of the asymmetry contribution can be obtained by comparing the present neutron potentials with proton potentials for  $^{56}\text{Fe}$  found in the literature [PP76]. There are a number of the latter, of varying quality both with respect to the underlying experimental data and to its interpretation. However, when the proton potential strengths are converted to volume-integrals-per-nucleon a pattern becomes evident. After neglecting several anomalous results and making corrections for the coulomb energy shift, there are ten reasonably consistent spherical proton potentials distributed between approximately 7 and 26 MeV. All of the  $J_v$  values of these potentials are larger than those given by the present ESOM but the energy dependence of the  $J_v$ 's is approximately the same as given by the ESOM. Thus, the proton potentials support the strong energy dependence of the  $J_v$  of the present SOM interpretations. It is well known that the asymmetry dependence can be expressed in the form  $J_v = J_v^0(1 \pm \xi \cdot \eta)$  where  $\eta = (N-Z)/A$ ,  $\xi$  is a constant, and "+" applies to proton potentials and "-" to neutron potentials [Lan62]. Thus the systematic magnitude



difference between  $^{56}\text{Fe}$  proton and neutron spherical potentials determines  $\xi$ . The present comparisons result in  $\xi = 0.46 \pm 0.12$ . The estimated relatively-large uncertainty is due to the scatter of the proton  $J_v$  values. This value of  $\xi$  is very consistent with the  $\xi = 0.43$  resulting from neutron studies of a range of tin isotopes [Smi95] and with the value  $\xi = 0.48$  suggested by the theory of nucleon-nucleon scattering ([TSW63], [TT67], [OP66], [GPT68], [GMP70]). It is not consistent with an  $\xi$  of approximately unity often reported in the literature. The latter are usually determined from potential comparisons over a wide mass range and include a simple mass dependence of  $J_v$  which is not readily distinguishable from the asymmetry contribution of approximately the same size. There is a  $J_w$  asymmetry dependence qualitatively similar to that of  $J_v$ . However, the relevant proton  $J_w$  values scatter by amounts that make quantitative assessments, such as above for  $J_v$ , unreliable. Thus they were not attempted. The above reflects an unusual situation, for  $^{56}\text{Fe}$  below  $\approx 30$  Mev neutron scattering data is more comprehensive and accurate than the proton-scattering data.

#### 5.11. Microscopic models

There have been several attempts to interpret neutron scattering from iron using microscopic models (e.g., refs. [Mel+83], [Ols+87], [Han+84]). The models have generally used the nuclear matter approach of Jeukenne, Lejeune and Mahaux [JLM77] with Reid's hard-core interaction [Rie68], or the folding model of Brieva and Rook [BR78] with the Hamada-Johnston interaction [HJ62]. Real and imaginary potentials were calculated from these microscopic models and then normalized to obtain the best description of the differential neutron elastic-scattering data. The real-potential normalization constants are close to unity but the imaginary-potential normalizations can significantly deviate from unity, particularly for the Brieva-Rook approach. The calculated results qualitatively agree with the measured neutron-scattering differential distributions (e.g., see refs. [Ols+87], [Han+84] and [Mel+83]), but tend to over-predict the total cross sections for lighter targets (i.e., for  $^{56}\text{Fe}$ ). In the microscopic studies reported thus far the approach of Jeukenne et al. [JLM77] appears to give the best results. The volume integrals,  $J_v$  and  $J_w$  predicted by these microscopic models can be compared with the respective quantities following from the present SOM interpretations with the results given in Table 5.11.1. All the microscopic calculations are at relatively high energies (at  $\approx 8 - 26$  MeV). The results calculated with the JLM model are very similar to those following from the present phenomenological interpretations at higher energies (e.g., above  $\approx 14$  MeV). The results obtained with the BR model are not quite as good, but still rather impressive. The comparisons of Table 5.11.1 suggest that the microscopic models will be less suitable at lower energies (e.g.,  $\leq 10$  MeV) as, for example,

Table 5.11.1. Comparison of SOM potential strengths,  $J_i$ , following from the present phenomenological interpretations with those predicted by microscopic optical models.  $J_i$  values are in units of MeV-fm<sup>3</sup>.

$E_n$ (MeV)	$J_v$			$J_w$		
	Exp.	JLM <sup>c</sup>	BR <sup>d</sup>	Exp.	JLM	BR
8.0	456.4 <sup>a</sup> 466.1 <sup>b</sup>	433.2 <sup>e</sup>	438.3 <sup>e</sup>	95.3 <sup>a</sup> 100.9 <sup>b</sup>	105.6 <sup>e</sup>	103.4 <sup>e</sup>
10.0	445.2 <sup>a</sup> 453.0 <sup>b</sup>	423.2 <sup>e</sup>	433.8 <sup>e</sup>	95.2 <sup>a</sup> 98.7 <sup>b</sup>	102.2 <sup>e</sup>	116.5 <sup>e</sup>
12.0	434.4 <sup>a</sup> 440.3 <sup>b</sup>	421.4 <sup>e</sup>	444.9 <sup>e</sup>	95.0 <sup>a</sup> 96.5 <sup>b</sup>	92.7 <sup>e</sup>	119.9 <sup>e</sup>
14.0	424.2 <sup>a</sup> 428.1 <sup>b</sup>	416.1 <sup>e</sup>	434.1 <sup>e</sup>	97.6 <sup>a</sup> 97.0 <sup>b</sup>	96.6 <sup>e</sup>	127.7 <sup>e</sup>
20.0	396.2 <sup>a</sup> 394.3 <sup>b</sup>	391.3 <sup>e</sup>	401.3 <sup>e</sup>	105.2 <sup>a</sup> 98.4 <sup>b</sup>	98.8 <sup>e</sup>	122.0 <sup>e</sup>
21.6	389.6 <sup>a</sup> 386.0 <sup>b</sup>	390.2 <sup>f</sup>	401.2 <sup>f</sup>	107.2 <sup>a</sup> 98.8 <sup>b</sup>	89.9 <sup>f</sup>	102.7 <sup>f</sup>
26.0	372.7 <sup>a</sup> 364.6 <sup>b</sup>	371.6 <sup>e</sup>	395.6 <sup>e</sup>	112.8 <sup>a</sup> 99.9 <sup>b</sup>	97.7 <sup>e</sup>	115.9 <sup>e</sup>

<sup>a</sup> predicted by the ISOM of Section 4.

<sup>b</sup> predicted by the ESOM of Section 4.

<sup>c</sup> the model of ref. [JLM77].

<sup>d</sup> the model of ref. [BR78].

<sup>e</sup> calculated value from ref. [Mel+83].

<sup>f</sup> calculated value from ref. [Ols+87].

the the energy dependence of  $J_v$  is not as great as indicated by the phenomenological models. Furthermore, the microscopic models indicate a strong volume-imaginary potential at low energies where there is no phenomenological support for such a concept. This may be a reflection of the omission of channel coupling in the microscopic-model studies. Such a trend has been noted previously in phenomenological studies where volume absorption is more prominent in spherical than collective models (e.g., compare refs. [ElK+82] and [Del+82]), and is consistent with the present work.

### 5.12. Dispersion effects

There are a number of indications in the above interpretations that dispersive effects are relevant. They result in a real-potential strength given by

$$J_v = J_{HF} + \frac{P}{\pi} \int_{-\infty}^{+\infty} \frac{J_{ws}(E')}{E - E'} dE', \quad (5.12.1)$$

where  $J_{HF}$  is the local-equivalent Hartree-Fock potential,  $J_{ws}$  is the strength of the surface imaginary potential, and  $P$  denotes the principal value of the integral [Sat83]. Use of Eq. 5.12.1 in the interpretation of the actual experimental data is thwarted by large fluctuations at the lower energies where the contribution of the integral is significant. However, one can qualitatively assess the effect of the dispersion integral by numerically considering pseudo data. This approach was taken here.

An equivalent-local Hartree-Fock (HF) "base" potential was assumed to have the geometries and the spin-orbit potential of the ISOM of Table 4.3.1. The HF real-potential strength was taken to be a linear representation of that of the ISOM over the energy range 15 to 25 MeV. At these higher energies dispersion contributions to the real potential should be small. The higher-energy branch of the imaginary strength of the ISOM was assumed to represent that of the "base" potential. These "base" potential parameters are given in Table 5.12.1. The use of ISOM geometries in this approximation may be mitigated by their possible sensitivity to dispersion effects, but they do form a reasonable base-line for subsequent assessments of relative changes due to the introduction of dispersion contributions.

With the above "base" potential,  $J_v$  of Eq. 5.12.1 was evaluated following the procedures of ref. [Smi94]. This method yields the ratio  $\lambda(E)$  defined by

$$\lambda(E) = \frac{\Delta J_v(E)}{J_{ws}(E)}, \quad (5.12.2)$$

where  $\Delta J_v$  is the surface component added to the HF potential strength

and  $J_{ws}$  is the surface-imaginary potential strength. The resulting  $\lambda(E)$  monotonically decreases from  $\approx 0.64$  at zero energy to very small values at  $\approx 15$  MeV and above. In other words, the contribution of the integral of Eq. 5.12.1 is large at low energies, and decreases to become insignificant at high energies. Using the "base" potential, and the dispersion contribution defined by  $\lambda(E)$ ,  $^{56}\text{Fe}$  pseudo elastic-scattering data was constructed with the SOM every MeV from zero to 25 MeV using methods analogous to those described in Appendix B. The differential cross sections were calculated at  $5^\circ$  intervals, and the cross-section uncertainties were taken to be 3% or 0.4 mb/sr, whichever was larger. The result is a pseudo-experimental elastic-scattering data base including known contributions from the dispersion integral, but free of the large low-energy fluctuations that haunt the actual experimental data.

The pseudo data was then least-square fitted using a simple spherical optical potential, devoid of dispersion contributions, in the manner described in Section 4. The resulting model parameters are compared with those of the "base" potential in Table 5.12.1. It is evident that the neglect of dispersion effects considerably changes the model parameters.  $J_v$  is significantly larger at low energies and has a greater energy dependence. Moreover, the behavior is quite similar to that of the ISOM of Table 4.3.1.  $r_v$  is increased at low energies and has a stronger energy dependence. Concurrently,  $a_v$  is generally decreased, particularly at low energies. The effect of the dispersion integral on the imaginary-potential parameters is less marked, with small changes in  $J_w$  and  $a_w$ . However,  $r_w$  is significantly increased at higher energies and conversely at lower energies. The entire fitting procedure was repeated including the dispersion contribution given by  $\lambda(E)$  in the model employed in the fitting. The resulting potential parameters were essentially identical to those of the "base" potential, as they should be.

The above simple exercise suggests that there are significant distortions of the parameters resulting from the fitting of the actual experimental data due to the neglect of dispersion effects. These distortions are only a partial explanation of some of the parameter behavior observed in the fitting; for example, the large increase in  $J_w$  at low energies can not be attributed to the neglect of dispersion effects alone. It was noted that total cross sections calculated with and without the dispersion contributions were quite similar above 8-10 MeV. However, the values calculated with dispersion effects were 10% or more smaller below several MeV. The smaller total cross sections at low energies are more consistent with experimental trends. The introduction of dispersion effects reduces the calculated s-wave strength functions by  $\approx 40\%$  and the p-wave values by  $\approx 25\%$ . The lower calculated strength-functions tend to be closer to the experimental values (see Table 5.7.1).

---

Table 5.12.1. Comparison of spherical optical-model potentials used in estimating dispersion effects, as described in the text. The nomenclature is the same as used in Section 4.

---

HF "Base" Potential	Potential Resulting from Fitting Pseudo-data
<hr/>	
Real Potential	
$J_v = 482.6 - 4.288 \cdot E$	$= 512.0 - 5.413 \cdot E + 0.00782 \cdot E^2$
$r_v = 1.300 - 0.0038 \cdot E$	$= 1.340 - 0.0052 \cdot E$
$a_v = 0.6338$	$= 0.5208 + 0.0123 \cdot E, \quad E < 8$
	$= 0.6139 + 0.00084 \cdot E, \quad E \geq 8$
Imaginary Potential	
$J_w = 95.98 - 0.0802 \cdot E$	$= 91.27 + 0.611 \cdot E, \quad E < 10$
	$= 99.22 - 0.234 \cdot E, \quad E \geq 10$
$r_w = 1.2600 - 0.0024 \cdot E$	$= 1.2261 + 0.0034 \cdot E, \quad E < 8$
	$= 1.2860 - 0.0036 \cdot E, \quad E \geq 8$
$a_w^* = 0.2586 + 0.0285 \cdot E -$	$= 0.2658 + 0.0253 \cdot E -$
$0.000589 \cdot E^2$	$0.000453 \cdot E^2$
Spin-orbit Potential	
(Same as the ISOM of Table 4.3.1)	

---

\* For convenience a quadratic representation of the values of the ISOM of Table 4.3.1 is used for the "base" potential.

---

Dispersion effects are generally most evident in the bound-energy regime where one can test potentials by comparing measured and calculated binding energies of particle and hole states. These are traditionally obtained from studies of (d,p) and (d,t) reactions, in the present case the reactions  $^{55}\text{Fe}(d,p)$  and  $^{57}\text{Fe}(d,t)$ .  $^{55}\text{Fe}$  is not stable so there are no  $^{55}\text{Fe}(d,p)$  results.  $^{57}\text{Fe}$  is a very minor isotope and the available  $^{57}\text{Fe}(d,t)$  information is only fragmentary. Due to this weak experimental knowledge, no attempt was made to make comparisons with binding energies calculated with the present models.

### 5.13. Summary comments

The scope and accuracy of the present experimental results enhance the understanding of neutron scattering from iron (essentially  $^{56}\text{Fe}$ ) from the lower-energy highly-fluctuating region to  $\approx 10$  MeV where the cross sections take on a relatively smooth energy dependence. These results, combined with those reported in the literature, provide unusual knowledge of neutron scattering from very low energies to more than 25 MeV. This is a region where changing physical effects are expected and one not accessible to charged-particle measurements. This knowledge of neutron scattering from  $^{56}\text{Fe}$  may well be a unique example of neutron scattering that is better known than charged-particle scattering, and this understanding offers an opportunity for detailed physical interpretations that was exploited.

The present work provides good SOM's and CCM's. The latter well describe the direct neutron interaction with  $^{56}\text{Fe}$ . However, the CCM results do not offer a clear choice between vibrational or rotational interactions. The latter concept may be very consistent with shell-model predictions but the neutron cross sections calculated with the alternate choices differ by only very small amounts. All of the present models have energy-dependent geometries, relatively large and strong energy dependencies of the real potential strengths, and remarkably large imaginary potential strengths at low energies. Some of these properties are partly attributable to dispersive effects and, for the SOM's, to the use of an inappropriate model. All of the models successfully unify the interpretations of high- and low-energy neutron processes in a manner not here-to-fore accomplished. The quadrupole deformation resulting from the present interpretations is somewhat larger than that suggested for proton processes, consistent with the core-coupling model. Volume-imaginary potentials remain an enigma with the interpretations suggesting small values above  $\approx 15$  MeV in the SOM context and smaller, if any, contributions in the context of the CCM's.

## ACKNOWLEDGEMENTS

The author is indebted to Dr. T. Burrows and Ms. V. McLane of the National Nuclear Data Center for their help in preparing the data for this work. The author is particularly indebted to Dr. D. Schmidt for making available his excellent scattering data prior to publication.

## APPENDIX A. PTB-DATA INTERPRETATIONS

A primary constituent of the data base used in the above model considerations is the experimental elastic-scattering results from PTB [Sch94]. That work appears to result in among the most accurate experimental values and gives particular attention to uncertainty specifications. The results span the incident-energy range  $\approx 9.5$  to 15 MeV in increments of  $\approx 0.5$  MeV, and with good angular coverage. Due to the scope and quality of this data set, it was separately studied in the context of the ISOM, CCVIB and CCR0T models. The objective was a phenomenological parameterization of this accurate data set, suitable for interpolation in energy and for extrapolation of the differential elastic-scattering data to other reaction types (e.g., to the total cross section). In addition, the quality of the data may illuminate physical properties not evident in the more general interpretations discussed above in the body of the report.

It was assumed that the geometric parameters of the models are energy independent. This is a reasonable assumption over the  $\approx 5.5$  MeV span of the data base. Volume absorption was ignored as the above general interpretations indicate that it is zero below  $\approx 12$  MeV and, at most, very small at 15 MeV. At 9 MeV and above compound-nucleus contributions to elastic scattering should be very small and thus they were neglected. Since this entire data set employed a detailed and common uncertainty philosophy, the parameters obtained by fitting at each incident energy were appropriately weighted by the  $\chi^2$  of the particular fit in order to obtain the general behavior (e.g., weighted averages were constructed of the geometric parameters obtained by fitting at each incident energy). That approach is often not rewarding when dealing with a data base consisting of components from diverse sources, each with different uncertainty philosophies.

With the above assumptions, ISOM, CCVIB and CCR0T parameter sets were determined by fitting, following the procedures set forth in the above report. In the course of the fitting there was a suggestion that small energy-dependent fluctuations remained in the data base even at these energies. They were manifest in systematic energy-dependent trends in the geometric parameters which, for example, tended to be different at 12 MeV and 14 MeV. The weighted averages of the geometric parameters were accepted for the overall parameterizations. It was also evident that the  $\chi^2$  surface is not very sensitive to the real-potential radius,  $r_v$ . This is not surprising due to the strong correlation between real-potential depth

and radius. However, in these cases the minimum of  $\chi^2$  with  $r_v$  is particularly broad and, as a consequence,  $r_v$  is not well defined.

The resulting potential-parameter sets are given in Tables A.1 to A.3. At the energies of these interpretations, the parameters sets are reasonably consistent with those of the comparable general models of the main report. The CCVIB and CCR0T parameters are very similar, with differences that are perhaps not significant. However, the ISOM parameters are quite different, particularly in the strengths and the imaginary-potential geometry. These are typical of the qualitative differences characteristic of comparisons of spherical and coupled-channels models, as discussed in the main body of the report and in Appendix B. All three parameter sets give reasonable descriptions of the elastic-scattering data base from which they were derived, as illustrated in Fig. A.1. The CCVIB and CCR0T models give essentially the same results. Both are descriptive of the measured data but for a modest under-prediction of the first minimum of the distribution at the lowest several energies. This discrepancy is far more pronounced for the ISOM results. The parameterizations were used to extrapolate the differential elastic-scattering data to the total cross sections with the results given in Table A.4. All three parameter sets give essentially the same total cross sections, with differences in the order of a percent. There is a similar agreement with the energy-average of the measured total cross sections of refs. [Cie+68] and [Lar80]. The two experimental total-cross-section data sets differ from one another by approximately the same amount as from the calculated results. This good agreement between measured and calculated total cross sections suggests that normalization of the PTB differential elastic-scattering data is excellent. Table A.4 indicates that the total cross section offers little guidance as to the choice of the parameter sets.

The direct inelastic excitation of the  $\gamma$ st  $2^+$  (847 keV) level in  $^{56}\text{Fe}$  is clearly inconsistent with the concept of the ISOM parameterization. Both CCVIB and CCR0T parameterizations employ a  $\beta_2 = 0.239$  as given in the literature [Ram+87], and both give essentially the same angle-integrated cross sections for the excitation of this level (see Table A.4). The inelastic-neutron angular distributions calculated with the CCVIB and CCR0T are quite similar to one another, and to the experimental data, as illustrated in Fig. A.2. Both sets of calculated inelastic-scattering results give angular dependencies that are very close to those indicated by the measured data but both sets may be slightly larger in magnitude than the comparable experimental values. Adjustments of  $\beta_2$  and/or the coupling schemes possibly could improve the agreement between measured and calculated inelastic-scattering results (particularly in respect to magnitude), as stated in Section 5.9 of the above report. Either of the coupled-channels parameterizations provide a reasonable extrapolation of the inelastic-scattering cross sections to



---

Table A.1. ISOM parameters developed from the PTB data base. Geometrical parameters are given in fermis, energies (E) in MeV, real and imaginary strengths as volume-integrals-per-nucleon in units of MeV-fm<sup>3</sup>, and the spin-orbit strength in MeV.

---

-----

Real Potential

$$J_v = 471.15 - 3.2421 \cdot E$$

$$r_v = 1.2590$$

$$a_v = 0.6133$$

Imaginary Potential

$$J_w = 92.91 - 0.2514 \cdot E$$

$$r_w = 1.1856$$

$$a_w = 0.5440$$

Spin-orbit Potential

$$V_{so} = 5.9099 - 0.015 \cdot E$$

$$r_{so} = 1.103$$

$$a_{so} = 0.560$$

---

---

Table A.2. CCVIB parameters developed from the PTB data base. Geometrical parameters are given in fermis, energies (E) in MeV, real and imaginary strengths as volume-integrals-per-nucleon in units of MeV-fm<sup>3</sup>, and the spin-orbit strength in MeV.

---

-----

Real Potential

$$J_v = 496.92 - 3.1716 \cdot E$$

$$r_v = 1.2792$$

$$a_v = 0.6801$$

Imaginary Potential

$$J_w = 64.30 + 1.7009 \cdot E$$

$$r_w = 1.2923$$

$$a_w = 0.4109$$

Spin-orbit Potential

$$V_{so} = 5.9099 - 0.015 \cdot E$$

$$r_{so} = 1.103$$

$$a_{so} = 0.560$$

Deformation

$$\beta_2 = 0.239$$

---

---

Table A.3. CCR0T parameters developed from the PTB data base. Geometrical parameters are given in fermis, energies (E) in MeV, real and imaginary strengths as volume-integrals-per-nucleon in units of MeV-fm<sup>3</sup>, and the spin-orbit strength in MeV.

---

-----  
Real Potential

$$J_v = 516.43 - 3.8982 \cdot E$$

$$r_v = 1.2710$$

$$a_v = 0.6664$$

Imaginary Potential

$$J_w = 65.28 + 1.6479 \cdot E$$

$$r_w = 1.2914$$

$$a_w = 0.3484$$

Spin-orbit Potential

$$V_{so} = 5.9099 - 0.015 \cdot E$$

$$r_{so} = 1.103$$

$$a_{so} = 0.560$$

Deformation

$$\beta_2 = 0.239$$

---

Table A.4. Comparison of cross sections calculated with the ISOM, CCROT and CCVIB models of Appendix A. Incident energies,  $E_n$ , are in MeV and cross sections,  $\sigma$ , in barns.  $\sigma_{inel}$  refers to the excitation of the yrast  $2^+$  level in  $^{56}\text{Fe}$ .

---

$E_n$	ISOM		CCROT			CCVIB		
	$\sigma_t$	$\sigma_{el}$	$\sigma_t$	$\sigma_{el}$	$\sigma_{inel}$	$\sigma_t$	$\sigma_{el}$	$\sigma_{inel}$
<hr/>								
9.41	3.140	1.672	3.175	1.682	0.122	3.176	1.676	0.117
9.97	3.053	1.595	3.085	1.606	0.117	3.086	1.600	0.113
10.53	2.967	1.520	2.997	1.532	0.112	3.000	1.526	0.109
11.00	2.895	1.458	2.924	1.470	0.109	2.929	1.466	0.106
11.42	2.833	1.405	2.864	1.418	0.106	2.869	1.415	0.103
11.96	2.756	1.340	2.788	1.354	0.102	2.795	1.352	0.100
12.46	2.689	1.284	2.722	1.298	0.098	2.730	1.297	0.097
13.07	2.612	1.221	2.647	1.234	0.095	2.657	1.236	0.093
13.63	2.547	1.167	2.584	1.180	0.091	2.595	1.184	0.090
14.09	2.498	1.127	2.537	1.140	0.088	2.549	1.145	0.087
14.58	2.449	1.088	2.491	1.101	0.086	2.504	1.108	0.084
15.20	2.396	1.045	2.440	1.059	0.082	2.455	1.066	0.081

---

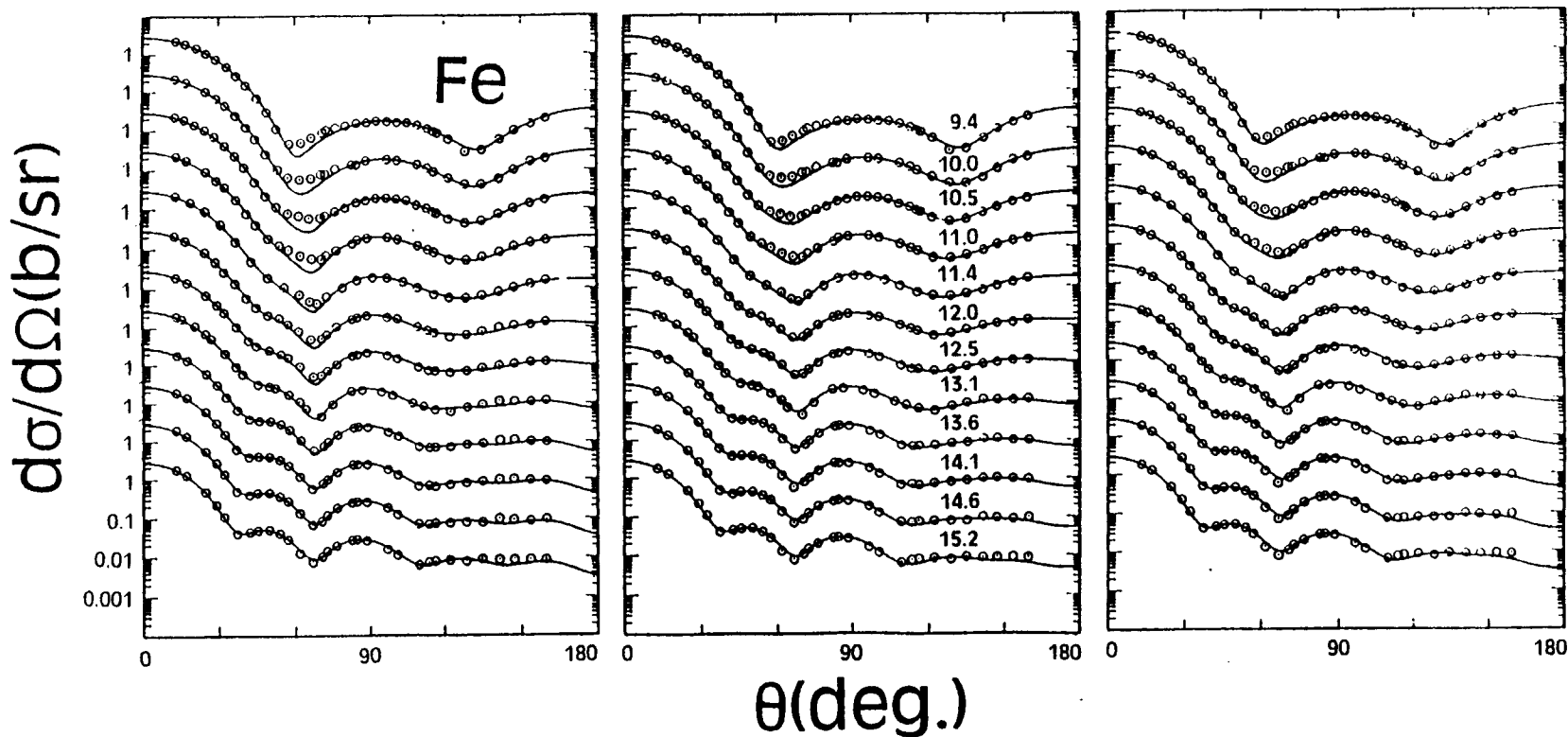


Fig. A.1. Comparison of calculated elastic scattering data (curves) with the PTB experimental results (symbols) [Sch94]. Approximate incident neutron energies (in MeV) are numerically noted in the center panel of the figure. The calculations of the left panel were obtained using the ISOM, the center panel using the CCVIB model and the right panel using the CCR0T model.

unmeasurable forward and backward angles.

The above suggests that either coupled-channels parameterization is a good vehicle for interpolating and extrapolating the PTB differential-scattering data. The data does not clearly indicate a preference for either the CCVIB or CCR0T. The simple spherical ISOM is less suitable, particularly in the context of inelastic scattering where it simply does not at all account for the experimental results. The deformations used in the coupled-channels calculations are quite large (i.e.,  $\beta_2 = 0.239$ ) and therefore the coupled-channel concepts employed here are probably more suitable than the frequently encountered DWBA methods.

## APPENDIX B. PSEUDO-DATA FITTING

In Section 4 the neutron interaction was modeled assuming the target  $^{56}\text{Fe}$  was both a spherical and a collective nucleus. The two types of resulting potentials are different. It is of interest to explore to what extent these variations are rooted in the different underlying physical assumptions. This was done by constructing a neutron pseudo-experimental data base using a simple rotational model with the parameters of Table B.1 and a target mass of 56. These "base" parameters are physically reasonable, with the real-potential strength decreasing with energy, as predicted by Hartree-Fock estimates, and the imaginary strength increasing as more channels open. Differential elastic-scattering cross sections were calculated every  $6^\circ$  from  $12^\circ$  to  $162^\circ$  using the "base" potential. Three percent or 0.4 mb uncertainties were assigned to the calculated values, whichever was larger. The calculations were made every 250 keV from 0.25 to 2 MeV, at every 500 keV from 2 to 5 MeV, at every 1 MeV from 5 to 8 MeV and at every 2 MeV from 8 to 20 MeV. These calculated results form a very comprehensive pseudo-experimental data set with an angle and energy scope and an accuracy considerably exceeding any actual experimental data found in the literature. For simplicity, only the shape-elastic cross sections were dealt with.

The elastic-scattering pseudo-experimental data was fitted in the manner described in Section 4, assuming a simple spherical potential. The resulting geometric parameters displayed considerable fluctuations near the threshold of the yrast ( $2^+$ ) state. However, by the time the energy increased to  $\approx 1.5$  MeV the parameters had settled to a relatively systematic behavior extending to the upper limit of 20 MeV. These higher-energy parameter trends were accepted in the successive steps of the fitting procedure. This is consistent with the interpretations of Section 4 as the lowest energy of the elastic-scattering data base used there was 1.5 MeV.

The SOM parameters resulting from the above fitting exercise are summarized in Table B.1, and the potential strengths illustrated in

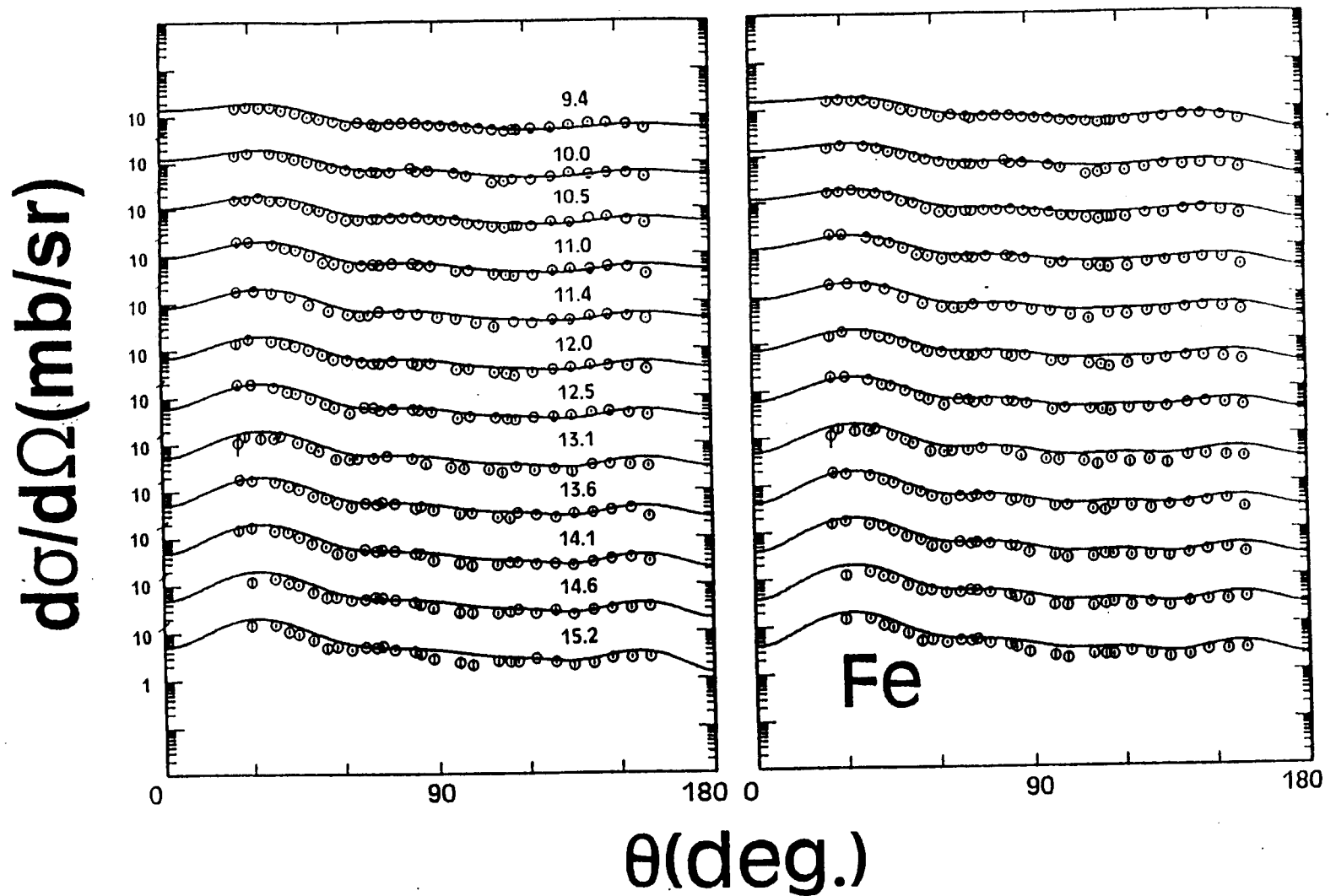


Fig. A.2. Comparison of calculated inelastic-scattering cross sections for the excitation of the 847 keV level (curves) with the PTB experimental results (symbols) [Sch94]. The nomenclature is the generally the same as for Fig. A.1 except that the incident energies are numerically cited in the left panel which displays the results of CCVIB calculations and the right panel the results of the CCROT model.

---

Table B.1. Potentials used in the pseudo-data fitting exercise. All geometries are in fermis and strengths,  $J_i$ , in volume integrals-per-nucleon (units of MeV-fm<sup>3</sup>), except for  $V_{so}$  which is in MeV.

---

CCROT "base: potential

SOM potential from fitting

Real potential

$$J_v = 480.6 - 3.004 \cdot E$$

$$= 481.5 - 3.980 \cdot E$$

$$r_v = 1.250$$

$$= 1.3102 - 0.002206 \cdot E$$

$$a_v = 0.650$$

$$= 0.6102$$

Imaginary potential

$$J_w = 86.76 + 2.169 \cdot E$$

$$= 151.6 - 4.7029 \cdot E + 0.18758 \cdot E^2$$

$$r_w = 1.260$$

$$= 1.1942$$

$$a_w = 0.500$$

$$= 0.4663 + 0.007229 \cdot E$$

Spin-orbit potential

$$V_{so} = 5.9099 - 0.015 \cdot E$$

( same )

$$r_{so} = 1.103$$

( same )

$$a_{so} = 0.560$$

( same )

$$\beta_2 = 0.239$$

( none )

Target <sup>56</sup>Fe

( same )

Yrast 850 (2<sup>+</sup>) keV state

( same )

---



Fig. B.1. The  $a_v$  of the SOM is somewhat smaller than that of the "base" potential, perhaps significantly so. The same trend is evident in comparisons of the ESOM and CCROT potentials of Section 4. The SOM  $r_v$  is larger than that of the "base" potential while the ESOM and CCROT values are approximately the same. However, as noted in Section 4,  $r_v$  is difficult to determine, particularly for  $^{56}\text{Fe}$ . The SOM  $r_w$  is smaller than that of the "base" potential, a trend consistent with that of the ESOM and CCROT. The SOM  $a_w$  increases with energy while the value of the "base" potential was assumed constant. The details are somewhat obscure but the SOM 20 MeV  $a_w$  value is larger than that of the "base" potential as for the comparison of ESOM and CCROT potentials. There is not a great deal of difference between the  $J_v$  values, as illustrated in Fig. B.1. However, that resulting from the SOM fitting has a slightly stronger energy dependence, following the trends of a comparison of ESOM and CCROT potentials ( $J_i$  calculations are slightly different for spherical and rotational models due to changes in  $\beta_2$  [Law92]). There is structure in the result of the SOM fitting at lower energies with a peak in  $J_v$  at the threshold of the inelastic channel. There was a tendency for the same effect in the actual data interpretations of Section 4. The SOM  $J_w$  is much larger than that of the "base" potential over most of the energy range, and has a different energy dependence. These differences are qualitatively similar to those between  $J_w$  values of the ESOM and CCROT potentials, and, in part, have to do with the explicit treatment of the yrast ( $2^+$ ) state in the rotational model. However, the rather sharp decreases in  $J_w$  with energy at low energies, characteristic of the actual interpretations of Section 4, are not reproduced.

The above exercise qualitatively supports some of the differences between ESOM and CCROT potentials obtained in the actual experimental interpretations of Section 4. The details depend on a number of factors, particularly on the angular range of the pseudo-data, the coupling scheme employed in the calculations and the algorithm chosen for determining the pseudo-experimental data uncertainties. Finally, the entire exercise was repeated assuming  $\beta_2 = 0.0$ ; i.e., a spherical "base" potential. With this starting point, the parameters deduced from the fitting agreed very closely with those of the input "base" potential.

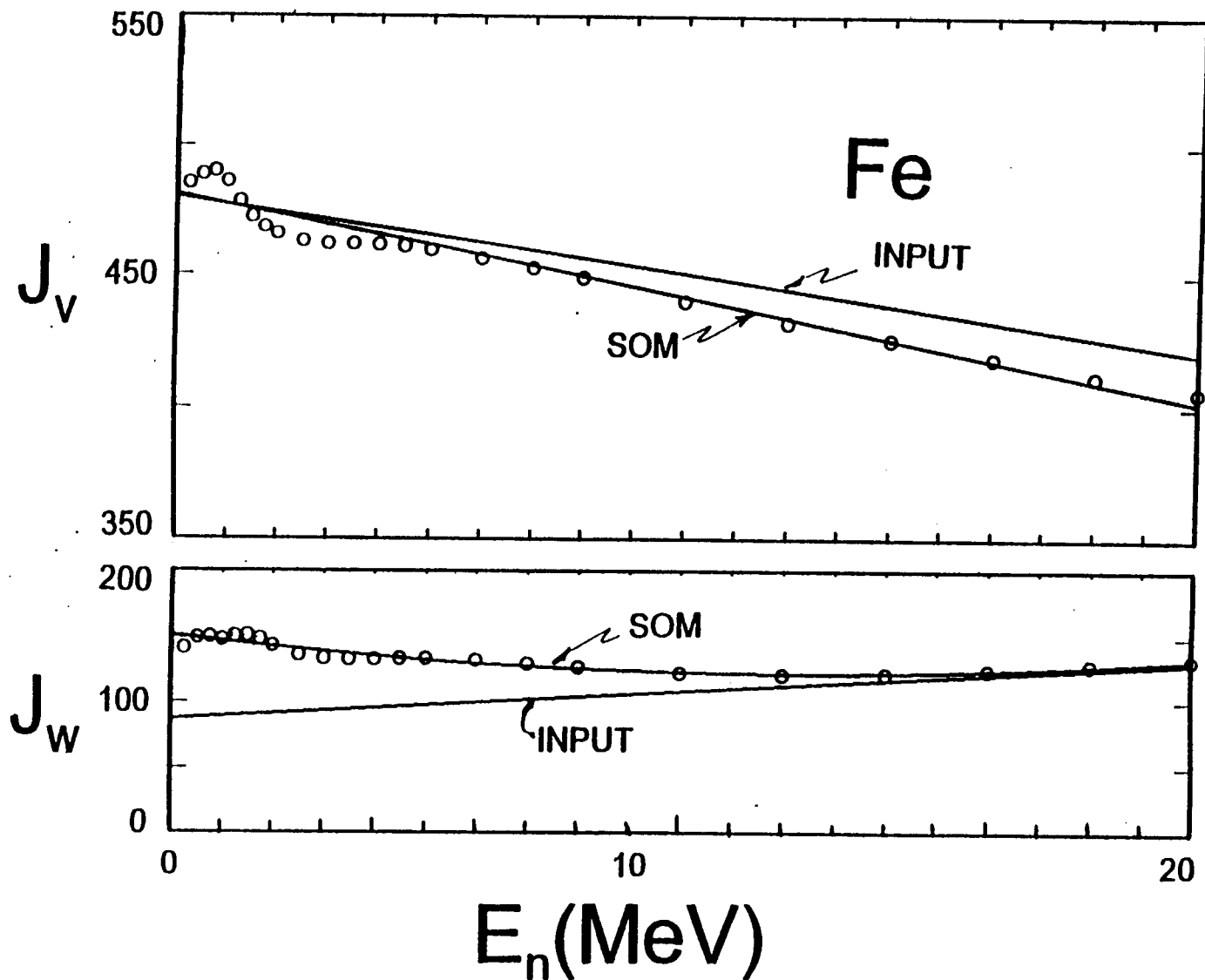


Fig. B.1. Comparison of real,  $J_v$ , and imaginary,  $J_w$ , potential strengths. Symbols indicate the results of SOM fitting of the pseudo data at individual energies. Curves "INPUT" were obtained using the "base" potential of Table B.1, and curves "SOM" indicate the SOM parameterization of Table B.1.  $J_i$  are in units of  $\text{MeV}\cdot\text{fm}^3$ .

## REFERENCES

- [AHW66] B. Antolkovic, B. Holmqvist and T. Wiedling, NEA Report, EANDC(OR)-51 (1966).
- [AY80] E. Arthur and P. Young, Los Alamos National Laboratory Report, LA-8626-MS (1981).
- [Bai+78] E. Bainum, R. W. Finlay, J. Rapaport, M. H. Hadizadeh, J. D. Carlson and J. R. Comfort, Nucl. Phys. A311 492 (1978).
- [Bar+68] E. Barnard, J. DeVilliers, C. Engelbrecht, D. Reitmann and A. B. Smith, Nucl. Phys. A118 321 (1968).
- [Bau+82] M. Bauer, H. Hernandez-Saldana, P. E. Hodgson and J. Quintanilla, J. Phys. G8 525 (1982).
- [Bla63] J. S. Blair, Direct interactions and nuclear reaction mechanisms p. 669 (Gordon and Breach, New York, 1963).
- [BLS71] P. Boschung, L. Lindlow and E. Shrader, Nucl. Phys. A161 593 (1971).
- [BR78] P. A. Brieva and J. R. Rook, Nucl. Phys. A307 493 (1978); see also Nucl. Phys. A291 299 (1977), Nucl. Phys. A291 317 (1977), and Nucl. Phys. A297 206 (1978).
- [Chi+90] S. Chiba, P. Guenther, R. Lawson and A. Smith, Phys. Rev. C42 2487 (1990).
- [Cie+68] S. Cierjacks, P. Forti, D. Kopsch, L. Kropp, J. Nebe and H. Unseld, Institute fur Angewandte Kernphysik Report, KFK-1000 (1968).
- [CL55] L. Cranberg and J. Levin, Proc. Inter. Conf. on Peaceful Uses of Atomic Energy (United Nations Press, New York, 1955).
- [CSL82] H. Conde, A. Smith and A. Lorenz, editors, Nuclear Standards File IAEA Tech. Report 227 (1992).
- [Coo+58] J. H. Coon, E. R. Graves and H. H. Barschall, Phys. Rev. 111 250 (1958).
- [Del+82] J. P. Delaroche, S. M. El-Kadi, P. P. Guss, C. E. Floyd and R. L. Walter, Nucl. Phys. A390 541 (1982).
- [Dro87] M. Drosig, IAEA Report, IAEA-TECDOC-410 (IAEA Press, Vienna, 1987).
- [ElK+82] S. M. El-Kadi, C. E. Nelson, F. O. Purser, R. L. Walter, A. Beyerle, C. R. Gould and L. M. Seagondollar, Nucl. Phys. A390 509 (1982).
- [EM69] A. J. Elwyn and J. E. Monahan, Nucl. Phys. A123 33 (1969).
- [Fer+77] J. C. Ferrer, J. D. Carlson, and J. Rapaport, Nucl. Phys. A275 325 (1977).
- [Flo+83] C. E. Floyd, P. P. Guss, R. C. Byrd, K. Murphy and R. L. Walter, Phys. Rev. C28 1498 (1983).
- [GC65] A. Gilbert and A. Cameron, Can. J. Phys. 43 1446 (1965).
- [GMP70] G. W. Greenlees, W. Makofske and G. J. Pyle, Phys. Rev. C1 1145 (1970).
- [Gon+87] Wang Gongquing, Zhu Jiabi and Zhan Jingen, Nucl. Data Sheets 50 255 (1987).
- [GPT68] G. W. Greenlees, G. J. Pyle and Y. C. Tang, Phys. Rev. 171 1115 (1968).
- [GT65] W. Gilboy and J. Towle, Nucl. Phys. 64 130 (1965).

- [Han+84] L. F. Hansen, F. S. Dietrich, B. A. Pohl, C. H. Poppe and C. Wang, Phys. Rev. C31 111 (1984).
- [HF52] W. Hauser and H. Feshbach, Phys. Rev. 87 362 (1952).
- [Hin+73] R. A. Hinrichs, D. Larson, B. M. Preedom, W. G. Love and F. Petrovich, Phys. Rev. C7 1981 (1973).
- [HJ62] T. Hamada and I. D. Johnston, Nucl. Phys. 34 382 (1962).
- [Hod71] P. E. Hodgson, Nuclear reactions and nuclear structure (Clarendon, Oxford, 1971).
- [Hol+69] B. Holmqvist et. al., Studsvik Report, AE-366 (1968).
- [JLM77] J. P. Jeukenne, A. Lejeune and C. Mahaux, Phys. Rev. C16 80 (1977); also Phys. Rev. C15 10 (1977).
- [Jun+87] Huo Junde, Hu. Dialing, Zhou Chunmei, Han Xiaoling, Hu Baohau and Wu Yaodong, Nucl. Data Sheets 51 1 (1987).
- [Kin68] W. E. Kinney, Oak Ridge National Laboratory Report, ORNL-TM-2052 (1968).
- [KP70] W. E. Kinney and F. G. Perey, Oak Ridge National Laboratory Report, ORNL-4515 (1970).
- [Lac+76] J. Lachkar, M. T. McEllistrem, G. Haouat, Y. Patin, J. Sigaud and F. Cocu, Phys. Rev. C14 933 (1976).
- [Lan62] A. M. Lane, Nucl. Phys. 35 676 (1962); also Phys. Rev. Lett. 8 171 (1962).
- [Lar80] D. Larson, Brookhaven National Laboratory Report, BNL-277 (1980).
- [Law92] R. D. Lawson, private communication (1992).
- [LVS81] M. J. Levine, E. K. Warburton and D. Schwalm, Phys. Rev. C23 244 (1981).
- [MBA75] V. A. Madsen, V. R. Brown and J. D. Anderson, Phys. Rev. C12 1205 (1975).
- [MDH81] S. Mughabghab, M. Divadeenam and N. Holden, Neutron cross sections (Academic, New York, 1981).
- [Mel+83] S. Mellema, R. W. Finlay, F. S. Dietrich and F. Petrovich, Phys. Rev. C28 2267 (1983).
- [Mol63] P. A. Moldauer, Nucl. Phys. 47 63 (1963).
- [Mol80] P. A. Moldauer, Nucl. Phys. A344 185 (1980).
- [Mol82] P. A. Moldauer, Spherical optical model code ABAREX, private communication 1982; modified by S. Chiba for elemental use.
- [Mol82A] P. A. Moldauer, Coupled-channels code ANLECIS, private communication (1982); a version of ECIS79 by J. Raynal [Ray79].
- [MR79] J. B. McGrory and S. Raman, Phys. Rev. C20 830 (1979).
- [NNDC] National Nuclear Data Center, Brookhaven National Laboratory, Upton, New York.
- [Ols+87] N. Olsson, B. Trostelle, E. Ramstrom, B. Holmqvist, and F. S. Dietrich, Nucl. Phys. A472 237 (1987).
- [OP66] S. Oaki and S. C. Park, Phys. Rev. 145 787 (1966).
- [OTR90] N. Olsson, B. Trostelle and E. Ramstrom, Nucl. Phys. A513 205 (1990).
- [Ped+88] R. S. Pedroni, C. R. Howell, G. M. Honore, H. G. Pfitzner, R. C. Byrd, R. L. Walter and J. P. Delaroche, Phys. Rev. C38 2052 (1988).

- [Per+77] F. G. Perey, G. T. Chapman, W. E. Kinney and C. M. Perey, Proc. Specialist's Mtg. on Neutron Data of Structural Materials for Fast Reactors, p. 530, ed. K. Boekhoff (Pergamon, Oxford, 1977).
- [PKM71] F. Perey, W. Kinney and R. Macklin, Proc. Conf. on Nucl. Sci. and Technology, Knoxville, eds. C. Johnson and J. Fowler (1971).
- [PP76] C. M. Perey and F. G. Perey, At. Data and Nucl. Data Tables 17 1 (1976).
- [Ram75] E. Almen-Ramstrom, Studsvik Report, AE-530 (1975).
- [Ram+87] S. Raman, C. H. Marlarkey, W. T. Miller, C. W. Nester Jr. and P. H. Stelson, At. Data Nucl. Data Tables, 36 1 (1987).
- [Ray79] J. Raynal, NEA memorandum (1979), unpublished; a later version of the code ECIS is documented in the report CEA-N-2772 (1994).
- [Rie68] R. V. Ried, Ann. Phys. 50 411 (1968).
- [RKF79] J. Rapaport, V. Kulkarni and R. W. Finlay, Nucl. Phys. A330 15 (1979).
- [RSL67] W. Rodgers, E. Shrader and J. Lindlow, Chicago Operations Office Report, COO-1573 (1967).
- [Sal81] M. Salama, Atomkernenergie 37 221 (1981).
- [Sat83] G. R. Satchler, Direct nuclear reactions (Clarendon, Oxford, 1983).
- [Sch94] D. Schmidt, Proc. Inter. Conf. on Nucl. Data for Sci. and Technology (Am. Nucl. Soc. Press, LaGrange, 1994); see also the Physikalisch Technische Bundesanstalt Report, PTB-N-20 (1994).
- [SG80] A. B. Smith and P. T. Guenther, Nucl. Sci. and Eng., 73 186 (1980).
- [SGS77] A. Smith, P. Guenher and R. Sjoblum, Nucl. Instr. and Methods, 140 397 (1977).
- [SLW66] A. Smith, D. Lister and J. Whalen, Proc. Paris Conf. on Nucl. Data (1966).
- [Smi+67] A. Smith, P. Guenher, R. Lasen, C. Nelson, P. Walker and J. Whalen, Nucl. Instr. and Methods, 50 277 (1967).
- [Smi91] A. B. Smith, Monte-carlo correction codes MONTEPHERE and MONTEPOLY, unpublished Argonne National Laboratory memorandum (1991).
- [Smi+92] A. B. Smith and P. T. Guenther, Argonne National Laboratory Report, ANL/NDM-127 (1992); S. Chiba, P. Guenther, A. Smith, M. Sugimoto and R. D. Lawson, Phys. Rev. C45 1260 (1992); C. Budtz-Jorgensen, P. Guenther, A. Smith and J. Whalen, Z. Phys. A306 265 (1982); and references cited therein.
- [Smi94] A. B. Smith, Nucl. Phys. A576 165 (1994).
- [Smi95] A. B. Smith, Nucl. Phys. A589 201 (1995).
- [Tom+70] Y. Tomita et al., Proc. Conf. on Nuclear Data for Fission Reactors, Helsinki (IAEA press, 1970).
- [TSW63] Y. C. Tang, E. Schmid and K. Wildermuth, Phys. Rev. 131 2631 (1963).
- [TT67] D. R. Thompson and Y. C. Tang, Phys. Rev. 159 806 (1967).
- [Vel+74] P. E. Velkey et al., Phys. Rev. C9 2181 (1974).

- [WG86] R. L. Walter and P. P. Guss, Proc. of Conf. on Nucl.  
Data for Basic and Applied Sci., eds. P. Young et al., Vol.  
2, p. 277 (Gordon and Breach, New York, 1986).
- [You86] P. G. Young, NEA Report, NEANDC-222U (1986).